Topological charge distributions of an interacting two-spin system

György Frank,[1,2] Dániel Varjas,[3,4] Péter Vrana,[5] Gergő Pintér,[1,6] and András Pályi[1,7]

[1]*Department of Theoretical Physics, Budapest University of Technology and Economics, H-1111 Budapest, Hungary*
[2]*MTA-BME Exotic Quantum Phases Group, Budapest University of Technology and Economics, H-1111 Budapest, Hungary*
[3]*QuTech and Kavli Institute of Nanoscience, Delft University of Technology, 2600 GA Delft, Netherlands*
[4]*Department of Physics, Stockholm University, AlbaNova University Center, 106 91 Stockholm, Sweden*
[5]*Institute of Mathematics, Budapest University of Technology and Economics, H-1111 Budapest, Hungary*
[6]*Institute of Mathematics, Eötvös Loránd University, Pázmány Péter sétány 1/c, H-1117 Budapest, Hungary*
[7]*MTA-BME Lendület Topology and Correlation Research Group, Budapest University of Technology and Economics, 1521 Budapest, Hungary*

(Received 4 February 2021; revised 24 November 2021; accepted 17 December 2021; published 12 January 2022)

Quantum systems are often described by parameter-dependent Hamiltonians. Points in parameter space where two levels are degenerate can carry a topological charge. Here we theoretically study an interacting two-spin system where the degeneracy points form a nodal loop or a nodal surface in the magnetic parameter space, similarly to such structures discovered in the band structure of topological semimetals. Key results of our work are that (1) we determine the topological charge distribution along these degeneracy geometries and (2) we show that these nonpointlike degeneracy patterns can be obtained not only by fine-tuning but they can be stabilized by spatial symmetries. Since simple spin systems such as the one studied here are ubiquitous in condensed-matter setups, we expect that our findings, and the physical consequences of these nontrivial degeneracy geometries, are testable in experiments with quantum dots, molecular magnets, and adatoms on metallic surfaces.

DOI: 10.1103/PhysRevB.105.035414

I. INTRODUCTION

Quantum systems are often described by parameter-dependent Hamiltonians, with many models incorporating multiple tunable parameters [1–7]. For example, the three Cartesian components of the external magnetic field provide $N = 3$ parameters in the Hamiltonian of an interacting multi-spin system [7–11].

Let us summarize a few *generic* features for the case when the only constraint on the parametrized Hamiltonian is its Hermiticity. In this case, it requires at least $N = 3$ parameters to find points in the parameter space where two of the energy levels are degenerate [12,13]. If the dimension of the parameter space is exactly $N = 3$, then the *generic* degeneracy points are isolated. If $N > 3$, then the degeneracy points form $(N - 3)$-dimensional geometrical patterns in the N-dimensional parameter space, e.g., lines in a four-dimensional parameter space, surfaces in a five-dimensional parameter space, etc. Moreover, in the vicinity of a generic isolated degeneracy point in a three-dimensional parameter space (a so-called *Weyl point*), the energy splitting between the two levels depends linearly on the distance from the Weyl point.

It is customary to associate a topological charge to a pointlike degeneracy in a three-dimensional parameter space [7,9,11,14]. For example, take a single localized electron in a magnetic (Zeeman) field,

$$H = \boldsymbol{B} \cdot \boldsymbol{S}, \tag{1}$$

where $\boldsymbol{B}$ is the magnetic field and $\boldsymbol{S}$ is the spin–1/2 vector operator, that is, 1/2 times the Pauli matrices. For simplicity, we use dimensionless quantities, i.e., we omit the Bohr magneton μ_B from the Hamiltonian. In this example, the degeneracy point is at the origin, $\boldsymbol{B}_0 = 0$. Calculating the surface integral of the ground-state Berry curvature vector field on a closed surface surrounding this degeneracy point yields 1, independent of the shape of the surface. For a closed surface whose interior does not contain the degeneracy point, this integral is zero. Using the analogy to electrostatics of a point charge and Gauss's law justifies the terminology that the degeneracy point carries unit topological charge. As electric charge is the source of electric field, we define topological charge as the source of Berry curvature.

Fine-tuning or the presence of symmetries can lead to anomalous, *nongeneric* situations when degeneracy points in a three-dimensional parameter space are (i) isolated but the energy splitting is not linear, but of higher order [15–18] or (ii) not isolated but they form a continuous line or surface [16,19–26]. These anomalous features have been demonstrated in electronic band structure models of three-dimensional solids, where the parameters are the Cartesian components of crystal momentum, and also in interacting spin systems with a three-dimensional magnetic parameter space [11].

In this paper, we consider the three-dimensional parameter space, and focus on case (ii), when either a degeneracy line or a degeneracy surface is present. As we illustrated above, the topological charge of an isolated degeneracy is concentrated in a single point and is characterized by the total charge. However, for an extended degeneracy line or degeneracy surface, it

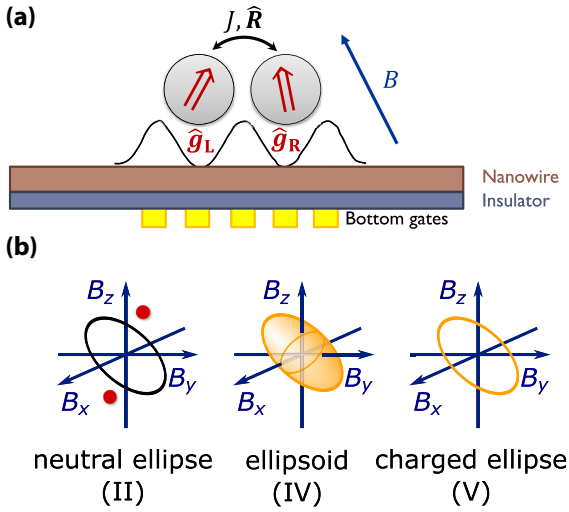

FIG. 1. Interacting two-spin system and its nonpointlike magnetic degeneracy patterns. (a) Two localized spinful electrons in a double quantum dot, in the presence of spin-orbit coupling, interacting with each other via exchange interaction (J, $\hat{\boldsymbol{R}}$), and an external magnetic (Zeeman) field $\boldsymbol{B}$ via g tensors $\hat{\boldsymbol{g}}_{\rm L}$ and $\hat{\boldsymbol{g}}_{\rm R}$. Figure shows one potential realization [7] defined in a nanowire (brown) by electrostatic gates (yellow). (b) Nonpointlike magnetic degeneracy patterns of the two-spin system. (II) Two degeneracy points with unit (+1) topological charge each (red) and a neutral degeneracy ellipse. (IV) Degeneracy ellipsoid surface carrying a total topological charge of +2. (V) Degeneracy ellipse carrying a total topological charge of +2. Classes (II), (IV), (V) were defined in Table I of Ref. [11].

is a natural question to ask: How is the net topological charge *distributed* on the line or surface? As the central result of this paper, we formulate the topological charge density on these higher dimensional manifolds using the analogy to electrostatics. In the line degeneracy case, we also show, in general, that any point with linear energy splitting in all transverse (nontangential) directions must be neutral.

As an experimental motivation and an illustrative example, we take the spin-orbit-coupled interacting two-spin problem we studied in the experiment of Ref. [7] and in the theory work Ref. [11], and we use the labels defined in Table I of the latter reference. The setup is illustrated in Fig. 1(a). A degeneracy line appears in the magnetic parameter space in cases (II) and (V), and a degeneracy surface appears in case (IV). The degeneracy patterns are sketched in Fig. 1(b), and introduced in more detail in Sec. II below.

For the neutral ellipse in case (II), we find that the topological charge distribution along the ellipse is identically zero. For the charged ellipse in case (V), the net topological charge +2 is evenly distributed between two opposite points of the degeneracy ellipse, and all further points of the ellipse are neutral. These results illustrate our general finding that points of a degeneracy line with linear energy splitting are always neutral. For the charged ellipsoid in case (IV), the net topological charge of +2 is distributed continuously, in striking similarity to how electric charge is distributed on the surface of a charged metallic ellipsoid. Furthermore, we show that these nonpointlike degeneracy geometries can be obtained not only by fine-tuning but they can be stabilized by spatial symmetries; we exemplify this for the case when the two-spin system has C_{3v} symmetry.

The rest of the paper is structured as follows. In Sec. II, we discuss the Hamiltonian of the spin-orbit coupled interacting two-spin model that we consider throughout this paper, and review our earlier results regarding the possible geometrical patterns formed by the ground-state degeneracy points of the magnetic parameter space. In what follows, we call the degeneracy patterns labeled (II), (IV), and (V) of Ref. [11] as the *nonpointlike* degeneracy patterns of the two-spin model. In Secs. III and IV, we present and derive the topological charge distributions characterizing these nonpointlike degeneracy patterns. We provide a discussion of our results and general analytical arguments in Sec. V, and conclude in Sec. VI.

II. SETUP AND BACKGROUND: SPIN-ORBIT-COUPLED TWO-SPIN SYSTEM

The physical system we describe in this paper is a spin-orbit-coupled double quantum dot in the (1,1) charge configuration, that is, when both quantum dots are occupied by a single electron. In the past two decades, this setup has been used as a workhorse for a multitude of experiments in the field of spin-based quantum information processing. For example, it was used to demonstrate Pauli blockade [27], and the latter has been utilized as a spin readout mechanism in electron spin resonance [28], electrically driven spin resonance [29], and gate-controlled two-qubit gates [30]. Our Fig. 1(a) shows such a double dot formed by bottom gates (gold) in a nanowire (brown), similar to those measured in, e.g., Refs. [7,31,32].

A recent experimental work [7] realized such a double quantum dot in an InAs semiconducting nanowire, where spin-orbit interaction is very significant. Spin-orbit interaction plays a very important role in the physics of double dots, in general, and spin-based quantum bits in particular. The experiment [7] focused on the singlet-triplet anticrossing of the Zeeman spectrum of the (1,1) charge configuration.

In the absence of spin-orbit coupling, the interacting two-spin system in a double dot subject to a homogeneous magnetic field $\boldsymbol{B}$ is described by the following well-known Hamiltonian:

$$H = \boldsymbol{B} \cdot g(\boldsymbol{S}_{\rm L} + \boldsymbol{S}_{\rm R}) + J\boldsymbol{S}_{\rm L} \cdot \boldsymbol{S}_{\rm R}. \tag{2}$$

Here, the first term is the Zeeman interaction with the external homogeneous magnetic field $\boldsymbol{B}$, where $\boldsymbol{S}_{\rm L}$ and $\boldsymbol{S}_{\rm R}$ are the spin vector operators represented by $1/2$ times the spin-$1/2$ Pauli matrices, g denotes the electronic g factor, and J is the strength of the Heisenberg exchange interaction.

The Hamiltonian of Eq. (2) is isotropic and its spectrum is well-known. At zero magnetic field, the ground state is the nondegenerate singlet, whereas the excited state is a threefold degenerate level with three triplet energy eigenstates. For any direction of the magnetic field, at the specific field value $B_0 = J/g$, the ground state becomes twofold degenerate, as the energy level of the singlet and one of the polarized triplets coincide. This implies that the points in the magnetic-field parameter space where the ground state is degenerate form a sphere of radius B_0.

This sphere of ground-state degeneracy points is dissolved immediately when the isotropy of the problem is broken by spin-orbit interaction. Modeling spin-orbit interaction in the interacting two-spin system is often done by the following generalization [7,11,33] of Eq. (2):

$$H = \boldsymbol{B} \cdot (\hat{\boldsymbol{g}}_{\mathrm{L}} \boldsymbol{S}_{\mathrm{L}} + \hat{\boldsymbol{g}}_{\mathrm{R}} \boldsymbol{S}_{\mathrm{R}}) + J \boldsymbol{S}_{\mathrm{L}} \cdot \hat{\boldsymbol{R}} \boldsymbol{S}_{\mathrm{R}}. \tag{3}$$

Here, the first term is the spin-orbit-affected Zeeman term, where $\hat{\boldsymbol{g}}_{\mathrm{L}}$ and $\hat{\boldsymbol{g}}_{\mathrm{R}}$ are the real-valued g tensors that are distorted by spin-orbit coupling with respect to their isotropic form in Eq. (2). The g tensors are not necessarily symmetric, but we assume that both have a positive determinant [11].

The second term in Eq. (3) is the exchange interaction between the two electrons, which deviates from the standard Heisenberg exchange of Eq. (2) due to spin-orbit interaction. In the second term of Eq. (3), $J > 0$ is the strength of the exchange interaction and $\hat{\boldsymbol{R}}$ is a real, 3×3 special orthogonal matrix accounting for the spin-orbit interaction in the exchange term. The origin of this Hamiltonian is discussed in detail in Refs. [7,11,33].

Note that numerous experiments have shown that g tensors of electrons confined in semiconductors can be tuned *in situ* by electric fields [31,34–37]. Therefore, we regard the spin-orbit-affected parameters, that is, the matrix elements of the g tensors, the exchange strength J, and the exchange rotation $\hat{\boldsymbol{R}}$, as tunable parameters. In what follows, we will refer to the magnetic-field space as the *parameter space* and will use the term *secondary parameters* for the further parameters of the Hamiltonian: the g tensors, the exchange strength J, and the exchange rotation $\hat{\boldsymbol{R}}$.

The key finding of Ref. [7] is that, even in this anisotropic configuration with spin-orbit interaction, there are always ground-state degeneracy points in the magnetic-field parameter space, guaranteed by topological properties of the Hamiltonian. If the secondary parameters are not fine-tuned, then two or six ground-state degeneracy points (Weyl points) remain [7] after switching on spin-orbit interaction, that is, upon moving from Eq. (2) to Eq. (3). However, as shown in Ref. [11], with appropriate fine-tuning of the secondary parameters, more exotic ground-state degeneracy patterns, including nodal lines and nodal surfaces, can be achieved. The complete list of seven different ground-state degeneracy patterns for this particular model is provided in Table I of Ref. [11] and are labeled as (I)–(VII).

Experimental observation of the seven ground-state degeneracy patterns in the spin-orbit-coupled two-spin system seems challenging but feasible. As mentioned above, fine-tuning of the secondary parameters of the model can be done by fine-tuning the confinement gate voltages of the quantum dots. Measuring the energy gap between the ground state and the first excited state can be done by, e.g., cotunneling spectroscopy [7], Landau-Zener spectroscopy [38,39], or two-tone spectroscopy [40–43], i.e., these techniques can reveal the existence and locations of Weyl points. Furthermore, the topological charge of the degeneracy points and the Berry curvature associated to the ground-state manifold can also be measured [10], as demonstrated with superconducting qubits [44]. The existence of these experimental tools serves as additional motivation to analyze the geometrical and topological features of the spin-orbit-coupled two-spin model and its exotic ground-state degeneracy patterns.

Throughout this paper, we will focus on the nonpointlike ground-state degeneracy patterns (II), (IV), and (V), which are illustrated in Fig. 1(b). Degeneracy pattern (II) consists of two Weyl points with topological charge $+1$ each, and a nodal loop (ellipse) which has a vanishing total topological charge. Degeneracy pattern (IV) describes the case when the ground state of the two-spin system is degenerate along an ellipsoid in the magnetic-field parameter space. This ellipsoid has a total topological charge of $+2$: If surrounded by a closed surface in the magnetic-field parameter space, the ground-state Chern number for that surface is $+2$. A special case of the ellipsoid is the isotropic situation described by the textbook Heisenberg exchange interaction, i.e., lack of spin-orbit interaction, as described by Eq. (2). For that special case, the ellipsoid simplifies to a sphere. Finally, degeneracy pattern (V) is a nodal loop, which has a total topological charge of $+2$.

The other degeneracy patterns have isolated point degeneracies. Pattern (I) and (VII) are the generic cases that do not require fine-tuning. These contain, respectively, 6 and 2 *ordinary Weyl points*, which have linear energy splitting in every direction and their topological charge is ± 1. Degeneracy pattern (III) has four points: two ordinary Weyl points with $+1$ charge and 2 *quadratic Weyl points*. The latter type of degeneracy has quadratic energy splitting in one specific direction and linear in the other directions; furthermore, it is neutral. Pattern (VI) has two *cubic Weyl points* with $+1$ charge each.

We close this section by recalling a few simple technical details regarding the spin-orbit-coupled two-spin system [11]. As noted earlier, we focus on the values of the magnetic field $\boldsymbol{B}_0$ where the ground state of the 4×4 Hamiltonian of Eq. (3) is twofold degenerate. Here we recall how to identify such magnetic degeneracy points analytically. If it holds for a unit vector $\boldsymbol{b}$ that

$$\boldsymbol{b}^{\mathrm{T}} \hat{\boldsymbol{g}}_{\mathrm{R}} \hat{\boldsymbol{R}}^{-1} \parallel \boldsymbol{b}^{\mathrm{T}} \hat{\boldsymbol{g}}_{\mathrm{L}}, \tag{4}$$

then there is a unique ground-state degeneracy point at a certain magnetic field $\boldsymbol{B}_+ = B_0 \boldsymbol{b}$ with $B_0 > 0$, and another one at $\boldsymbol{B}_- = -B_0 \boldsymbol{b}$. (Note that in our notation, $\parallel$ includes that the two vectors point to the same direction.) In turn, condition Eq. (4) is fulfilled if and only if $\boldsymbol{b}$ is a left eigenvector of the matrix

$$\hat{\boldsymbol{M}} = \hat{\boldsymbol{g}}_{\mathrm{L}} \hat{\boldsymbol{R}} \hat{\boldsymbol{g}}_{\mathrm{R}}^{-1}, \tag{5}$$

corresponding to a positive eigenvalue a. The absolute value of the magnetic field where the ground-state degeneracy occurs is

$$B_0 = \left(1 + \frac{1}{a}\right) \frac{J}{2 g_{\mathrm{R}}}, \tag{6}$$

where $g_{\mathrm{R}} = |\hat{\boldsymbol{g}}_{\mathrm{R}}^{\mathrm{T}} \boldsymbol{b}|$ (see Appendix C of Ref. [11]).

The above condition Eq. (4) is sufficient to guarantee the existence of two degeneracy points. We do not have a rigorous proof that Eq. (4) is also a necessary condition, but an extensive numerical search for degeneracy points found no counterexample, so we conjecture that it is.

The matrix $\hat{\boldsymbol{M}}$ defined in Eq. (5) is a 3×3 nonsymmetric real-valued matrix with positive determinant. The possible

degeneracy geometries are classified by its eigenstructure, i.e., the Jordan normal form of this matrix, see Table I in Ref. [11]. As shown there, the degeneracy points can be isolated, as in the electronic dispersion relation of a Weyl semimetal [4] or multi-Weyl semimetal [15], or they can form lines or surfaces, as in nodal-loop [21] or nodal-surface [22] semimetals.

In Ref. [11], we have already described these nonpointlike degeneracy patterns, and have established their total topological charge. In this paper, we address the question for line and surface degeneracies in general: How is their topological charge distributed along them? To answer this question, we use the two-spin system as a demonstrating example, but we also provide proofs in Appendices E and G for the general results of the line and surface degeneracies in quantum systems.

There are well-known analogies between electrostatics and geometric properties of parameter-dependent energy eigenstates: The electric field distribution created by a charged object is analogous to the Berry curvature in the vicinity of a degeneracy pattern, and the total charge of a charged object is the surface integral of the field for an arbitrary closed surface enclosing the object, much like the topological charge (Chern number) of a degeneracy pattern is the surface integral of the Berry curvature for an arbitrary surface surrounding that pattern. Can we define and compute a quantity in the quantum-mechanical setting that is analogous to the spatial (linear, surface) charge distribution of electrostatics?

III. LINEAR CHARGE DENSITY ALONG DEGENERATE LINES

To answer this question, we follow intuition from classical electrostatics. Since in our two-spin problem the degeneracy lines are closed loops, we take such an example from electrostatics.

As shown in Fig. 2, consider a loop l (blue), chosen to be circular with radius R for concreteness, parametrized by the path length variable $s \in [0, 2\pi R)$. Assume that this loop has a linear electrostatic charge distribution $\nu(s)$. The charge creates an electric field $\boldsymbol{E}(\boldsymbol{r})$. Can we deduce the linear charge density if only the induced electric field is known? Yes, in the following way:

$$\frac{\nu(s)}{\varepsilon_0} = \lim_{r\to 0} \int_0^{2\pi} d\vartheta\, \boldsymbol{E}(\boldsymbol{p}_r(s,\vartheta)) \cdot (\partial_\vartheta \boldsymbol{p}_r \times \partial_s \boldsymbol{p}_r)_{s,\vartheta}. \quad (7)$$

In this formula, $\boldsymbol{p}_r : [0, 2\pi R) \times [0, 2\pi) \to \mathbb{R}^3$ is the parametrization of a torus surrounding the loop as shown in Fig. 2, with $s \in [0, 2\pi R)$ used as the *longitude path length* and $\vartheta \in [0, 2\pi)$ used as the *meridian angle* of the torus. Furthermore, r is the meridian radius characterizing the thickness of the torus, that is, $r \to 0$ corresponds the thickness shrinking and the torus surrounding the loop infinitely tightly. Note that the dimension of s is a length (meter) whereas ϑ is an angle parameter hence is dimensionless.

In other words, Eq. (7) expresses that the distribution of the electric flux density on the torus provides an increasingly accurate picture of the charge density $\nu(s)$, as the torus radius is shrinking and the torus tightens around the charged loop. We prove this classical electrostatics relation Eq. (7) in Appendix A.

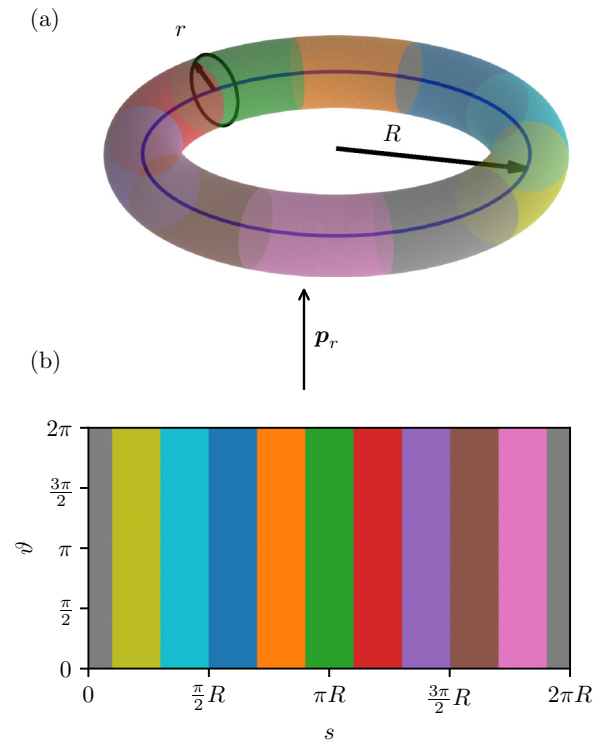

FIG. 2. Inferring the linear charge density of a charged loop from the electric field it creates. (a) Charged loop (blue) and a torus (colored) enclosing the loop, with meridian radius r. (b) The torus is parametrized by the map $\boldsymbol{p}_r : [0, 2\pi R) \times [0, 2\pi) \to \mathbb{R}^3$, using the longitude path length s and the meridian angle θ. The electric flux density on a torus reveals the linear charge density of the loop as meridian radius of the torus shrinks to zero, $r \to 0$, see Eq. (7).

Using the relation of Eq. (7), we identify the linear topological charge density along a degeneracy line. Patterns (II) and (V) are degeneracy loops (ellipses), hence we can again surround any of them by a shrinking torus, described by the parametrization $\boldsymbol{p}_r(s, \vartheta)$, where s has the dimension of magnetic field (Tesla) and ϑ is dimensionless. For an isolated degeneracy point, the ground-state topological charge or Chern number associated to the point reads

$$\mathcal{Q} = \frac{1}{2\pi} \int_S d\boldsymbol{A} \cdot \boldsymbol{\mathcal{B}}, \quad (8)$$

where the integral is calculated for a closed surface S enclosing the isolated degeneracy point, and $\boldsymbol{\mathcal{B}}$ is the Berry curvature vector field associated to the the ground-state wave function $\psi_0(\boldsymbol{B})$ defined as

$$\boldsymbol{\mathcal{B}}(\boldsymbol{B}) = i\langle \nabla_{\boldsymbol{B}} \psi_0(\boldsymbol{B})| \times |\nabla_{\boldsymbol{B}} \psi_0(\boldsymbol{B})\rangle, \quad (9)$$

or writing componentwise

$$\mathcal{B}_i(\boldsymbol{B}) = i\epsilon_{ijk} \langle \partial_{B_j} \psi_0 | \partial_{B_k} \psi_0 \rangle. \quad (10)$$

Therefore, for a degeneracy line, the formula revealing the linear topological charge density reads

$$\nu(s) = \frac{1}{2\pi} \lim_{r\to 0} \int_0^{2\pi} d\vartheta\, \boldsymbol{\mathcal{B}}(\boldsymbol{p}_r(s,\vartheta)) \cdot (\partial_\vartheta \boldsymbol{p}_r \times \partial_s \boldsymbol{p}_r)_{s,\vartheta}. \quad (11)$$

This is the quantity that we study in the following.

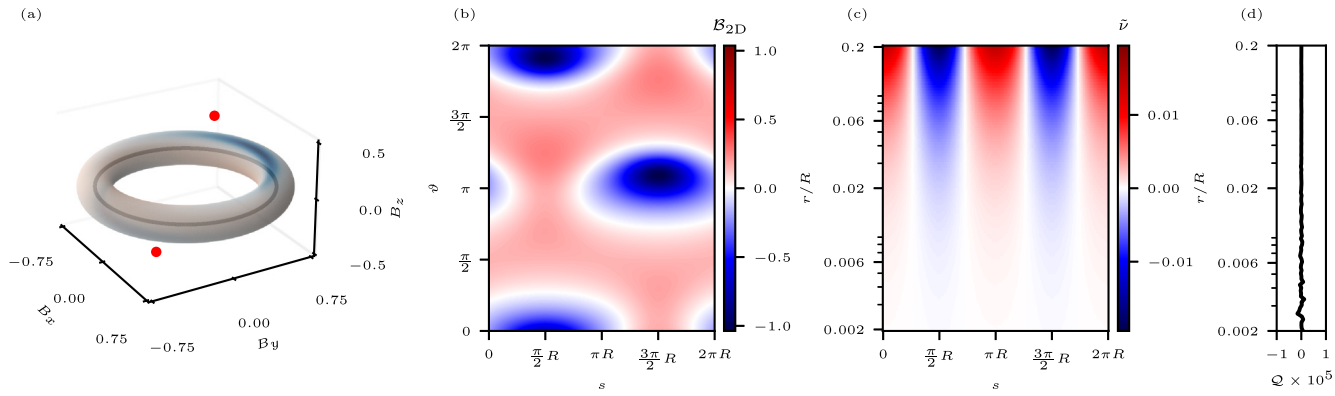

FIG. 3. Neutral degeneracy ellipse has vanishing linear topological charge distribution. (a) Berry flux density $\mathcal{B}_n$ (temperature map) on the surface of a torus surrounding a neutral degeneracy circle (black). Meridian radius, $r/R = 0.2$ (b) Two-dimensional Berry curvature $\mathcal{B}_{2D}(s, \vartheta)$ [Eq. (12)] on the preimage of the torus, i.e., as a function of longitude path length s and meridian angle ϑ. (c) Apparent linear topological charge density $\tilde{\nu}_r(s)$ [Eq. (13)] as function of longitude path length s and meridian radius r. As $r \to 0$, this function converges to the constant zero function (white), showing that the linear topological charge density vanishes, $\nu(s) = 0$. (d) A benchmark for the numerical integration: Numerically evaluated ground-state Chern number $\mathcal{Q}$ on the torus, as function of the meridian radius r. Numerical error grows slightly as $r \to 0$, due to the divergence of the Berry curvature in the vicinity of the degeneracy circle, but it remains well below 10^{-5} even for the smallest r values considered.

For future reference, we introduce the *two-dimensional (2D) Berry curvature* $\mathcal{B}_{2D}$ via

$$\mathcal{B}_{2D}(s, \vartheta) = \boldsymbol{\mathcal{B}}(\boldsymbol{p}_r(s, \vartheta)) \cdot (\partial_\vartheta \boldsymbol{p}_r \times \partial_s \boldsymbol{p}_r)_{s,\vartheta}, \tag{12}$$

i.e., the integrand in Eq. (11). We also introduce the *apparent topological charge density* $\tilde{\nu}_r(s)$, which is the right-hand side of Eq. (11), without taking the limit $r \to 0$:

$$\tilde{\nu}_r(s) = \frac{1}{2\pi} \int_0^{2\pi} d\vartheta \, \mathcal{B}_{2D}(s, \vartheta), \tag{13}$$

related to the charge density defined above as

$$\nu(s) = \lim_{r \to 0} \tilde{\nu}_r(s). \tag{14}$$

Since we use the Hamiltonian of Eq. (3) depending on dimensionless parameters $\boldsymbol{B}$ as our starting point, all these newly introduced quantities are also dimensionless. Reinstating physical dimensions in Eq. (3) is done by multiplying the first term with the Bohr magneton and reinterpreting $\boldsymbol{B}$ as a magnetic field and J as an energy. Then, the physical dimension of the Berry curvature and the Berry flux density is magnetic field^{-2}, whereas the dimension of the 2D Berry curvature, the apparent topological charge density, and the topological charge density is magnetic field^{-1}.

A. Pattern (II): Neutral ellipse

First, we consider the neutral ellipse degeneracy pattern (II) in Fig. 1(b). For this pattern, having zero total charge, one can envision two qualitatively different scenarios: (a) the charge distribution is identically zero at all points of the ellipse and (b) there is a nonzero linear charge density along the ellipse, but the negative and positive contributions cancel each other when added up for the entire ellipse. Speculation based on classical electrostatics intuition actually suggest scenario (b): If we think of the ellipse as a globally charge-neutral metal, then the two point charges outside the ellipse would polarize the ellipse (cf. the interesting analogy with electrostatics in Sec. IV).

Here, we provide evidence that scenario (a) is the case; the local charge distribution along the degeneracy ellipse vanishes. This is the first key result of this paper. This conclusion will be drawn from Fig. 3(c), but let us arrive there through a few intermediate steps.

In Fig. 3(a), we show the degeneracy patterns, two red points, and a black ellipse. We use the specific choice of parameters where the g tensors are

$$\hat{\boldsymbol{g}}_{\mathrm{L,II}} = \begin{pmatrix} 2 & 0 & 0 \\ 0 & 2 & 0 \\ 0 & 1 & 4 \end{pmatrix}, \quad \hat{\boldsymbol{g}}_{\mathrm{R,II}} = \mathbb{1}_{3\times 3}, \tag{15}$$

and the exchange interaction is characterized by $J_{\mathrm{II}} = 1$ and $\hat{\boldsymbol{R}}_{\mathrm{II}} = \mathbb{1}_{3\times 3}$. For simplicity, energy and magnetic field are dimensionless, unless noted otherwise.

The total topological charge carried by the red degeneracy points in Fig. 3(a) is $+2$. These degeneracy points are located at opposite magnetic fields,

$$\boldsymbol{B}_\pm = \pm \frac{\sqrt{5}}{8} \begin{pmatrix} 0 \\ 1 \\ 2 \end{pmatrix}, \tag{16}$$

and each of them carries a topological charge $+1$. The degeneracy ellipse shown as the black loop in Fig. 3 is actually a circle in the xy plane for this parameter set, centered at the origin, with radius $R = \frac{3}{4}$.

Figure 3(a) shows the Berry flux density on a torus surrounding the degeneracy circle. The Berry flux density is defined as the normal-to-surface component of the Berry curvature vector field. For example, for point $\boldsymbol{B}$ on the torus, the Berry flux density reads

$$\mathcal{B}_n(\boldsymbol{B}) = \boldsymbol{\mathcal{B}}(\boldsymbol{B}) \cdot \boldsymbol{n}(\boldsymbol{B}) \quad (\boldsymbol{B} \in \text{torus}), \tag{17}$$

where $\boldsymbol{n}(\boldsymbol{B})$ is the normal vector of the torus at point $\boldsymbol{B}$. The torus in Fig. 3(a) is colored according to the nonzero

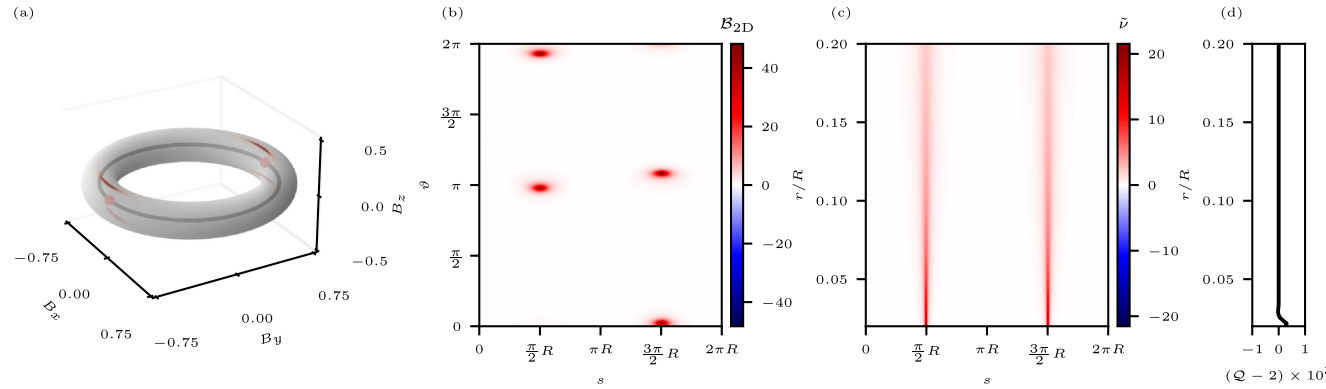

FIG. 4. Charged degeneracy ellipse has two charged points. (a) Berry flux density $\mathcal{B}_n$ (temperature map) on the surface of a torus surrounding a charged degeneracy circle (black). Meridian radius, $r/R = 0.2$ (b) Two-dimensional Berry curvature $\mathcal{B}_{2D}(s, \vartheta)$ [Eq. (12)] on the preimage of the torus, i.e., as a function of longitude path length s and meridian angle ϑ. (c) Apparent linear topological charge density $\tilde{\nu}_r(s)$ [Eq. (13)], as function of longitude path length s and meridian radius r. As $r \to 0$, this function converges to the constant zero function (white), showing that the linear topological charge density vanishes, $\nu(s) = 0$. (d) A benchmark for the numerical integration: Numerically evaluated ground-state Chern number on the torus, as function of the meridian radius r. Numerical error grows slightly as $r \to 0$, but it remains well below 10^{-3} even for the smallest r values considered.

Berry flux density. (Numerical techniques to obtain Fig. 3 are described in Appendix B.)

On the way toward the linear topological charge density, to be expressed via Eq. (11), we specify the parametrization of the torus surrounding the degeneracy line as

$$\boldsymbol{p}_r(s, \vartheta) = R\boldsymbol{e}_{\text{rad}}(s) + r[\cos\vartheta\, \boldsymbol{e}_z + \sin\vartheta\, \boldsymbol{e}_{\text{rad}}(s)], \tag{18}$$

with

$$\boldsymbol{e}_{\text{rad}}(s) = \begin{pmatrix} \cos(s/R) \\ \sin(s/R) \\ 0 \end{pmatrix}, \quad \boldsymbol{e}_z = \begin{pmatrix} 0 \\ 0 \\ 1 \end{pmatrix}. \tag{19}$$

Note that the normal vector of the torus can be expressed from the parametrization via

$$\boldsymbol{n}(\boldsymbol{p}_r(s, \vartheta)) = \frac{\partial_\vartheta \boldsymbol{p}_r \times \partial_s \boldsymbol{p}_r}{|\partial_\vartheta \boldsymbol{p}_r \times \partial_s \boldsymbol{p}_r|}. \tag{20}$$

With the parametrization in Eq. (18), in Fig. 3(b) we plot the 2D Berry curvature $\mathcal{B}_{2D}$ [see Eq. (12)] on the torus, with meridian radius $r = 0.2R$. The data in Fig. 3(b) is used to infer the linear topological charge density by numerically performing the integration over parameter ϑ and dividing by 2π to obtain the apparent charge density $\tilde{\nu}_r(s)$, and then taking the limit $r \to 0$. The apparent charge density as function of s and r is shown in Fig. 3(c). Although the value of the apparent charge density is nonzero for finite r, it does converge to zero for all values of s as $r \to 0$. This is numerical evidence that the degeneracy circle is charge neutral. To illustrate the accuracy of our result shown in Fig. 3(c), we numerically evaluate the ground-state Chern number $\mathcal{Q}$ on the torus as the function of the meridian radius r, by integrating the apparent charge density over the longitude path length s. The result, shown in Fig. 3(d), is indeed zero, exhibiting a numerical error less than 10^{-5}, illustrating that our numerical procedure is rather accurate.

Up to now, we considered a specific parameter set, and we performed numerical calculations for that special case. This leads us to the finding that the neutral ellipse has an everywhere-vanishing linear charge density. Does this hold only for this special case or is it generic for any neutral degeneracy ellipse within the spin-orbit-coupled two-spin model? We claim that the latter is true, and we outline the proof in Sec. V A.

B. Pattern (V): Charged ellipse

Next we consider the charged ellipse degeneracy pattern (V) in Fig. 1. The question is: How is the topological charge distributed along the ellipse? Using the method of the previous subsection, we show that the topological charge is concentrated at two opposite points of the ellipse, i.e., it is not continuously distributed along the ellipse. This is the second key result of this paper.

The example parameter set we use consists of g tensors

$$\hat{\boldsymbol{g}}_{\text{L,V}} = \begin{pmatrix} 2 & 0 & 0 \\ 0 & 2 & 0 \\ 0 & 1 & 2 \end{pmatrix}, \quad \hat{\boldsymbol{g}}_{\text{R,V}} = \mathbb{1}_{3\times 3}, \tag{21}$$

and the interaction is described by $J_{\text{V}} = 1$ and $\hat{\boldsymbol{R}}_{\text{V}} = \mathbb{1}_{3\times 3}$. The degeneracy ellipse is a circle with radius $R = \frac{3}{4}$ again, shown as a black line in Fig. 4(a).

Figure 4 (in analogy with Fig. 3) shows (a) the Berry flux density $\mathcal{B}_n$ on a torus surrounding the degeneracy circle, (b) the two-dimensional Berry curvature $\mathcal{B}_{2D}(s, \vartheta)$ on the preimage $[0, 2\pi R) \times [0, 2\pi)$ of the torus, (c) the apparent topological charge density $\tilde{\nu}_r(s)$ of the degeneracy circle, and (d) the numerically evaluated ground-state Chern number on the torus.

Figures 4(a) and 4(b) reveal a remarkable difference compared to Figs. 3(a) and 3(b): from Figs. 4(a) and 4(b), the Berry flux is concentrated in narrow regions (red spots) in the neighborhoods of two opposite points of the ellipse. Figure 4(c) suggests that the linear topological charge density, which corresponds to the plotted data $\tilde{\nu}_r(s)$ in the $r \to 0$ limit, consists of two Dirac deltas: the degeneracy circle is neutral in all points except two discrete points opposite to each other,

each carrying a topological charge of +1. In Sec. V A, this numerical evidence is supported by analytical results.

Figure 4(d) shows that the numerical error of the Chern number is below 10^{-3}, illustrating the accuracy of our numerical procedure. The feature that the error grows as the radius decreases is rather natural: For a smaller radius, the Berry flux gets more focused on a smaller area, hence our numerical integration using an equidistant grid on the preimage of the torus gets less accurate.

The direction of the charged points is $(0, 1, 0)^{\mathrm{T}}$, as determined by the Jordan decomposition of $\hat{\boldsymbol{M}}$, according to Eq. (C8). From Eq. (6), the position of these points is expressed as

$$\boldsymbol{B}_{\pm} = \pm\frac{3}{4}\begin{pmatrix}0\\1\\0\end{pmatrix}. \tag{22}$$

This result is in agreement with Fig. 4(c), where the charge density has two peaks at $s \in \{\frac{\pi}{2}R, \frac{3\pi}{2}R\}$.

Figure 4(b) shows pronounced peaks of the two-dimensional Berry curvature. These peaks appear because at each charged degeneracy point there are two opposite directions perpendicular to the tangent vector of the degeneracy circle in which the energy splitting grows quadratically as we move away from the circle, and the Berry flux density is typically greater where the splitting is smaller.

For both degeneracy points, we determine these directions analytically using Eq. (D25), and we find $(0, -1, 6)^{\mathrm{T}}$. This feature appears in the (s, ϑ) torus of Fig. 4(b) as red spots where the flux density is high; the spot locations can be determined analytically as

$$\begin{aligned}
(s_1, \vartheta_1) &= \left(\frac{\pi}{2}R, \pi - \tan^{-1}\frac{1}{6}\right),\\
(s_2, \vartheta_2) &= \left(\frac{\pi}{2}R, 2\pi - \tan^{-1}\frac{1}{6}\right),\\
(s_3, \vartheta_3) &= \left(\frac{3\pi}{2}R, \pi + \tan^{-1}\frac{1}{6}\right),\\
(s_4, \vartheta_4) &= \left(\frac{3\pi}{2}R, \tan^{-1}\frac{1}{6}\right),
\end{aligned} \tag{23}$$

matching the peaks seen in the numerical data.

To conclude, in this section we provided numerical evidence that the neutral degeneracy ellipse, pattern (II) of [11], has vanishing linear topological charge density, whereas the charged degeneracy ellipse, pattern (V) of [11], has all its topological charge focused in two opposite points of the ellipse. Even though the numerical results are obtained here for a specific choice of secondary parameters (g-tensors, exchange strength J and exchange rotation matrix $\hat{\boldsymbol{R}}$), the statements are general, see Sec. V A for the outline of the analytical proof. For example, if the secondary parameters are changed with respect to those in section III A, such that the resulting matrix $\hat{\boldsymbol{M}}$ still has the eigenpattern (II), then the degeneracy circle generically deforms into an ellipse, but all of its points remain charge-neutral. Results of section III B are generalized analogously. For details of these generalizations, we refer to Sec. V A.

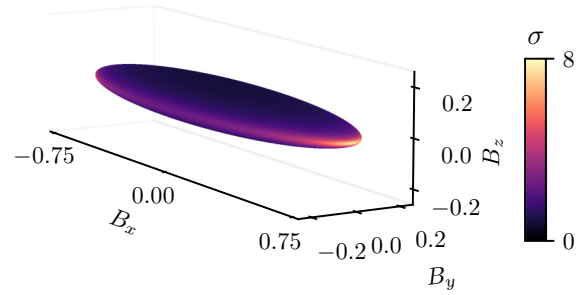

FIG. 5. Topological surface charge distribution on a degeneracy ellipsoid. See Sec. IV for parameter values. This topological charge distribution is the same as the electric charge distribution on the surface of a charged conducting ellipsoid.

IV. PATTERN (IV): CONTINOUS SURFACE CHARGE DISTRIBUTION ON AN ELLIPSOID

Consider now the degeneracy pattern (IV) from Fig. 1, the charged ellipsoid. Again, we will follow the electrostatics analogy to determine the surface topological charge distribution on this ellipsoid, see also Ref. [45]. In electrostatics the surface charge density $\sigma(\boldsymbol{r}_S)$ of surface S and the electric field $\boldsymbol{E}(\boldsymbol{r})$ created by the surface charge density are related by the following formula:

$$\frac{\sigma(\boldsymbol{r}_S)}{\varepsilon_0} = E_n(\boldsymbol{r}_{S+}) - E_n(\boldsymbol{r}_{S-}), \tag{24}$$

where $E_n(\boldsymbol{r}_{S+})(E_n(\boldsymbol{r}_{S-}))$ is the normal component of the electric field outside (inside) the surface at point $\boldsymbol{r}_S$ on the surface. Analogously, the surface topological charge density of the degeneracy ellipsoid S is related to the Berry curvature vector field via

$$\sigma(\boldsymbol{B}_S) = \frac{1}{2\pi}[\mathcal{B}_n(\boldsymbol{B}_{S+}) - \mathcal{B}_n(\boldsymbol{B}_{S-})], \tag{25}$$

where $\boldsymbol{B}_S$ is a point of the degeneracy surface.

Figure 5 shows this surface topological charge distribution $\sigma(\boldsymbol{B}_S)$ for the example parameter set with g tensors

$$\hat{\boldsymbol{g}}_{\mathrm{L,IV}} = \begin{pmatrix}2&0&0\\0&6&0\\0&0&18\end{pmatrix}, \quad \hat{\boldsymbol{g}}_{\mathrm{R,IV}} = \begin{pmatrix}1&0&0\\0&3&0\\0&0&9\end{pmatrix}, \tag{26}$$

and interaction described by $J_{\mathrm{IV}} = 1$ and $\hat{\boldsymbol{R}}_{\mathrm{IV}} = \mathbb{1}_{3\times3}$. With these parameters, the degeneracy ellipsoid has its principal axes aligned with the (B_x, B_y, B_z) reference frame. The semiaxes of the ellipsoid are

$$\alpha = \frac{3}{4}, \quad \beta = \frac{1}{4}, \quad \gamma = \frac{1}{12}. \tag{27}$$

In contrast to the result of Sec. III B, Fig. 5 shows a continuous charge distribution, which reads

$$\sigma(\boldsymbol{B}_S) = \frac{1}{2\pi\alpha\beta\gamma}\frac{1}{\sqrt{\frac{B_{Sx}^2}{\alpha^4} + \frac{B_{Sy}^2}{\beta^4} + \frac{B_{Sz}^2}{\gamma^4}}}. \tag{28}$$

This formula is obtained from the general result for the surface topological charge distribution:

$$\sigma(\boldsymbol{B}_S) = \frac{a \det \hat{\boldsymbol{g}}_R}{\pi(a+1)\left|\hat{\boldsymbol{g}}_R \hat{\boldsymbol{g}}_R^T \boldsymbol{B}_S\right|}. \tag{29}$$

Here, a is the only eigenvalue of the matrix $\hat{\boldsymbol{M}} = a \cdot \mathbb{1}_{3\times 3}$ [11]. Equation (29), which is the third key result of this paper, is derived in Appendix G.

Interestingly, the surface charge density in Eq. (28) has the same functional form as the electrical charge distribution of an electrically charged conducting ellipsoid [46]. Figure 5 exhibits the curvature effect known from electrostatics: The greater the curvature of the surface, the greater the topological charge density. A further similarity is that the Berry curvature inside the ellipsoid is zero, similarly to the electric field inside a charged ideal conductor. A difference, however, is that the Berry curvature in our example exits the surface radially with respect to the origin (i.e., it is proportional to $\boldsymbol{B}/B$), in contrast to the electric field which exits the conductor's surface in the surface normal direction [i.e., it is proportional to $\boldsymbol{n}(\boldsymbol{B})$]. Another difference is that the curl of the Berry curvature is nonzero [45], however, the curl of the electric field induced by the charged conductor vanishes.

Given a degeneracy surface in a three-dimensional parameter space, is it a generic feature that it carries a continuous topological surface charge density? Here we argue that it is. Such a degeneracy surface divides the parameter space to two disjoint regions—in our example, the inside and outside of the ellipsoid. The ground state changes continuously in both regions as the function of the parameters, generically implying a nonzero and continuous Berry curvature vector fields in both regions separately. But at the degeneracy surface, the ground state changes suddenly—in our example, from a singletlike state at the inside and a tripletlike state at the outside—and hence the Berry curvature also jumps, leading to a finite surface charge density according to Eq. (25).

V. DISCUSSION

A. Topological charge density vanishes for rank-2 points of degeneracy lines

In this section, we outline analytical results that support the numerical evidence of topological charge distributions studied in Sec. III. To this end, we define the *rank* of degeneracy points, establish the ranks of the degeneracy points forming the linear degeneracy patterns studied in Sec. III, and relate the rank of a degeneracy point to the topological charge of that point. In particular, we find that a rank-2 degeneracy point embedded in a linear degeneracy pattern carries no topological charge.

The *effective g tensor* $\hat{\boldsymbol{g}}_{\text{eff}}(\boldsymbol{B}_0)$ of a degeneracy point $\boldsymbol{B}_0$ is a 3×3 real matrix that characterizes the Hamiltonian in the parameter-space vicinity of the degeneracy point $\boldsymbol{B}_0$, focusing on the two levels that are degenerate at the degeneracy point. Formally, we introduce the *relative parameter vector* $\delta\boldsymbol{B} = \boldsymbol{B} - \boldsymbol{B}_0$ measured from the degeneracy point, project the Hamiltonian $H(\boldsymbol{B}_0 + \delta\boldsymbol{B})$ to the two-dimensional ground-state subspace of the degeneracy point $\boldsymbol{B}_0$ using an arbitrary orthonormal basis $(|0\rangle, |1\rangle)$, and express that the projected Hamiltonian in terms of Pauli matrices $\boldsymbol{\tau} = (\tau_x, \tau_y, \tau_z)$, e.g., $\tau_z = \frac{1}{2}(|0\rangle\langle 0| - |1\rangle\langle 1|)$, leading to the form [11]

$$H_p(\delta\boldsymbol{B}) = \delta\boldsymbol{B} \cdot \hat{\boldsymbol{g}}_{\text{eff}}(\boldsymbol{B}_0)\,\boldsymbol{\tau}. \tag{30}$$

Here, we have omitted the projected $H_p(\boldsymbol{B}_0)$, since it is proportional to the 2×2 unit matrix, owing to the degeneracy of the relevant two-dimensional subspace at $\boldsymbol{B}_0$. By the *rank* of a degeneracy point $\boldsymbol{B}_0$, we mean the matrix rank of the effective g tensor of that degeneracy point. Even though the effective g tensor depends on the choice of the basis $(|0\rangle, |1\rangle)$, its determinant and rank do not.

In Appendix D 1, we show that all degeneracy points of the neutral degeneracy ellipse are rank 2. Furthermore, in Appendix D 2 we show that in the charged degeneracy ellipse, the two points where the Berry flux density is concentrated in Fig. 4 are rank 1, and all other degeneracy points are rank 2. Finally, in Appendix E, we prove that the linear topological charge density at a rank-2 degeneracy point of a line degeneracy is zero, supporting the numerical evidence seen in Figs. 3(c) and 4(c). We also observe that the electrostatic analogy is not perfect: While the local charge density vanishes, hence there is no source of the Berry curvature on rank-2 degeneracy lines, there is always a linelike π flux tube along the degeneracy; for details, see Appendix E.

It is tempting to think about the charged ellipse degeneracy pattern (V) as a result of fine-tuning pattern (II): Upon tuning the secondary parameters (g tensors, exchange parameters), two charged points of pattern (II) merge with the neutral degeneracy ellipse of pattern (II), forming the charged degeneracy ellipse of pattern (V). (Note the related discussion on the conversion between Weyl point and nodal lines in band structures [47].) This picture is reinforced by the fact that pattern (V) is less stable than pattern (II), signalled by their stability codimensions 4 and 3, respectively (see Table I. of Ref. [11]). Furthermore, in Appendix C 2, we show an example where tuning a single parameter explicitly leads to two Weyl points merging with the neutral degeneracy ellipse.

B. Symmetries can stabilize nongeneric degeneracy patterns

Nongeneric band degeneracy points and patterns in solids can be stabilized by the presence of symmetries [15,23]. Here, we show that interacting spin systems are similar: Nongeneric degeneracy points can be stabilized by symmetries. This is the fourth (and final) key result of this paper.

We focus on a special case, when the two-spin system described by Eq. (3) has C_{3v} symmetry, and leave it for future work to explore further symmetry groups. We show that in this case, pattern (II) with two Weyl points and the neutral degeneracy circle is stabilized, even though it is unstable (codimension 3, see Table I in Ref. [11]) without the symmetry constraint.

Consider the case when the Hamiltonian is invariant under the isometries of group C_{3v}, which are generated by the threefold rotation $\mathcal{R}$ around the z axis and the reflection on the xz plane, $\mathcal{M}$. These isometries are represented by the 3×3 matrices

$$\mathcal{R} = \begin{pmatrix} \cos\frac{2\pi}{3} & -\sin\frac{2\pi}{3} & 0 \\ \sin\frac{2\pi}{3} & \cos\frac{2\pi}{3} & 0 \\ 0 & 0 & 1 \end{pmatrix} \tag{31}$$

and

$$\mathcal{M} = \begin{pmatrix} -1 & 0 & 0 \\ 0 & 1 & 0 \\ 0 & 0 & -1 \end{pmatrix} \tag{32}$$

on the pseudovectors (or axial vectors) appearing in the Hamiltonian of Eq. (3), i.e., the magnetic field $\boldsymbol{B}$ and the electron spins $\boldsymbol{S}_L$ and $\boldsymbol{S}_R$.

The presence of spatial symmetries is formalized as $H(\boldsymbol{B}, \boldsymbol{S}_L, \boldsymbol{S}_R) = H(\mathcal{R}\boldsymbol{B}, \mathcal{R}\boldsymbol{S}_L, \mathcal{R}\boldsymbol{S}_R)$ and $H(\boldsymbol{B}, \boldsymbol{S}_L, \boldsymbol{S}_R) = H(\mathcal{M}\boldsymbol{B}, \mathcal{M}\boldsymbol{S}_L, \mathcal{M}\boldsymbol{S}_R)$. These conditions restrict the forms of $\hat{\boldsymbol{g}}_L$, $\hat{\boldsymbol{g}}_R$, and $\boldsymbol{R}$, in particular, $\hat{\boldsymbol{g}}_L = \mathrm{diag}(g_{Lx}, g_{Lx}, g_{Lz})$, $\hat{\boldsymbol{g}}_R = \mathrm{diag}(g_{Rx}, g_{Rx}, g_{Rz})$, and $\boldsymbol{R} = \mathbb{1}_{3\times 3}$ or $\boldsymbol{R} = \mathrm{diag}(-1, -1, 1)$. For concreteness, we still assume positive determinants for the g tensors, which implies $g_{Lz}, g_{Rz} > 0$.

Combining these symmetry constraints with the definition in Eq. (5) leads to $\hat{\boldsymbol{M}} = \mathrm{diag}(a, a, b)$, where $b > 0$ and a might be either positive or negative. This matrix $\hat{\boldsymbol{M}}$ is its own Jordan normal form, so we can directly apply the Jordan classification in Table I of Ref. [11] to determine the degeneracy patterns arising in the magnetic parameter space. For $a < 0$, we find eigenpattern (VII), which has two Weyl points. For $a > 0$, we find eigenpattern (II), with two Weyl points and a neutral ellipse (circle, in this case), as studied in Sec. III A. Remarkably, as long as the C_{3v} symmetry is intact, the neutral ellipse survives without fine-tuning. In other words, the degeneracy pattern (II), which is unstable in the absence of symmetries, and hence is characterized by a positive codimension, becomes stable with zero codimension in the presence of C_{3v} symmetry.

C. Topological charge distributions in various quantum systems

The topological charge distribution along 1D or 2D degeneracy geometries in a 3D parameter space, which we studied throughout this paper, is a very natural and intuitive concept due to the strong analogy with electrostatics. So far, it has been rarely discussed and studied in the literature [45], but we expect an increasing interest in this concept for the following reasons.

(1) Recent theoretical and experimental works have revealed nonpointlike degeneracy patterns (nodal lines, nodal surfaces) in electronic band structures, which are topologically charged in the same sense as the nodal lines and nodal surfaces in our work. For a theoretical work predicting charged nodal lines, see Ref. [48]. For a theoretical-experimental study discovering a charged nodal surface, see Ref. [49]. In those systems as well, it is natural to ask how the topological charge is distributed along the nonpointlike degeneracy pattern. We expect that similar features will be analyzed in topologically nontrivial band structures of other quasiparticles as well, such as magnons and phonons. We regard our paper as an initial step in this direction.

(2) We expect further advancements in the field of controlled quantum systems, such that nonpointlike degeneracy structures and their topological charge distributions will be studied in theory and in experiment. A prominent example besides the interacting spin systems studied in our paper is the field of multiterminal Josephson junctions (e.g., Ref. [50]), where nodal-loop degeneracy patterns in the space of control parameters (gate voltages, magnetic fluxes) have been predicted. We expect that in such setups, an appropriate level of control of quantum states will be achieved, and thereby the Berry curvature and the topological charge density of the nodal loop will actually be measured.

(3) We anticipate a general mathematical classification of degeneracy points (both for pointlike and for nonpointlike degeneracy patterns) of multi-parameter-dependent Hamiltonians, where the concept of the topological charge density will play an important role. This anticipation is based on similar classification schemes for band structures (e.g., Table I in Ref. [51]), and our own preliminary unpublished results in that direction.

VI. CONCLUSIONS

We have exemplified the concepts of linear topological charge density and surface topological charge density through the example of a simple parameter-dependent quantum system, the spin-orbit-coupled two-spin problem where the parameters are the Cartesian components of the magnetic field acting on the spins. We have shown that the neutral degeneracy ellipse has vanishing topological charge density in all of its points, whereas the charged degeneracy ellipse has a charge distribution that is concentrated in two opposite points in the magnetic-field parameter space. Moreover, we have shown that the surface topological charge density of the degeneracy ellipse is continuous, and this charge density is identical to the surface charge density of a charged conducting ellipsoid. We extended these results by proving that, in general, the linear topological charge density is zero for line degeneracies with linear splitting in transverse directions, and the surface topological density is nonzero for surface degeneracies splitting the parameter space into two disjoint regions.

We have also shown that if the two-spin system has certain spatial symmetries, then this can stabilize an otherwise unstable, nongeneric degeneracy pattern, e.g., a neutral circle.

The nodal loops and surfaces are fragile for breaking the fine-tuning or symmetries which protect them. It is also true for the topological charge density. However, if we measure the Berry curvature of the system at a finite distance from the degeneracy, i.e., we look at the flux density on a thick torus in the parameter space surrounding a broken degeneracy ellipse [Figs. 3(b) and 4(b)], we don't observe any abrupt change. This robustness gives possibility to the experimental validation of our results.

The topological features described in this paper have numerous physical consequences, e.g., they determine the experimentally measurable Berry curvature [10,44,52], and also influence dynamical properties, such as paramagnetic resonance [28], Landau–Zener-type processes [38,39], and quantized frequency conversion [53,54]. Hence, we expect that our findings are testable in few-spin experiments, e.g., using quantum dots [7,11,35], molecular magnets [8,9,55], or adatoms on metallic surfaces [56,57].

ACKNOWLEDGMENTS

We acknowledge fruitful discussions with Y. Qian, A. Schnyder, H. Weng, and G. Zaránd. This work was supported

by the National Research Development and Innovation Office of Hungary within the Quantum Technology National Excellence Program (Project No. 2017-1.2.1-NKP-2017-00001), under OTKA Grants No. 124723 and No. 132146, and under the BME Nanotechnology and Materials Science TKP2020 IE grant (Grant No. BME IE-NAT TKP2020). D.V. was supported by NWO VIDI Grant No. 680-47-53, the Swedish Research Council (VR), and the Knut and Alice Wallenberg Foundation.

Gy.F. and A.P. formulated the project and wrote the initial draft of the paper. A.P. acquired funding, and managed the project. Gy.F. performed analytical and numerical calculations with assistance from A.P. and D.V., G.P., and P.V. consulted on differential-geometric aspects of the work. Gy.F. and D.V. produced the figures. All authors discussed the results and took part in writing the paper.

APPENDIX A: PROOFS OF EQ. (7)

1. First proof

In the main text, Eq. (7) expresses the linear charge density $\nu(s)$ of a charged loop in terms of the electric field $\boldsymbol{E}(\boldsymbol{r})$ created by the loop. Here, we provide an elementary proof of that result.

Consider a cylindrical section of the torus, together with its top base and bottom base, surrounding a section of the degeneracy circle in Fig. 2(a). Without loss of generality, we can take the section defined by the interval $s \in [0, s_0]$ with $0 < s_0 < 2\pi R$. From Gauss's law, the total charge enclosed by the cylinder is expressed from the electric field as

$$\frac{1}{\varepsilon_0}\int_0^{s_0} ds\nu(s) = \int_{\text{cylinder}} d\boldsymbol{A}\cdot\boldsymbol{E}. \tag{A1}$$

Up to now, we assume that the cylinder has a nonzero meridian radius r. Splitting the cylinder's surface integral to its three parts, we obtain

$$\frac{1}{\varepsilon_0}\int_0^{s_0} ds\nu(s) = \int_{\text{top base}} d\boldsymbol{A}\cdot\boldsymbol{E} + \int_{\text{bottom base}} d\boldsymbol{A}\cdot\boldsymbol{E} + \int_{\text{side}} d\boldsymbol{A}\cdot\boldsymbol{E}. \tag{A2}$$

For $r \to 0$, the top and bottom base contributions converge to zero (see below); hence we find

$$\frac{1}{\varepsilon_0}\int_0^{s_0} ds\nu(s) = \lim_{r\to 0}\int_{\text{side}} d\boldsymbol{A}\cdot\boldsymbol{E}. \tag{A3}$$

Using the parametrization $\boldsymbol{p}_r(s,\vartheta)$ of the main text, this can be written as

$$\frac{1}{\varepsilon_0}\int_0^{s_0} ds\nu(s) = \lim_{r\to 0}\int_0^{s_0} ds \times \int_0^{2\pi} d\vartheta \boldsymbol{E}(\boldsymbol{p}_r(s,\vartheta))\cdot[\partial_\vartheta \boldsymbol{p}_r \times \partial_s \boldsymbol{p}_r]_{s,\vartheta}. \tag{A4}$$

Assuming that the limit and the s integral can be exchanged, and considering that the boundaries of the s integral were arbitrary, we arrive to Eq. (7).

In the remaining part of this subsection, we prove that the flux contributions of the top and bottom bases approach zero as the radius r of the cylindrical section of the torus approaches zero. To prove this, we consider a rather general setting depicted in Fig. 6. Here, the red curve is a charged wire, parametrized as $\boldsymbol{x}(s) = (x(s), y(s), z(s))$ by its path length s, such that its left end corresponds to $s = 0$. The linear charge density of the wire is $\nu(s)$. Our goal is to show that the electric flux piercing the disk (blue) of radius r at $s = 0$, chosen to be perpendicular to the wire, converges to zero as the radius r approaches zero. This in turn ensures that the top-base and bottom-base integrals in the preceding paragraph vanish in the limit $r \to 0$.

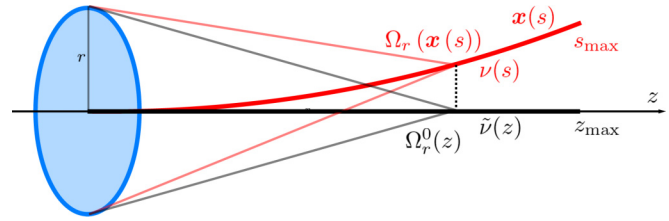

FIG. 6. Electric flux created by a charged wire (red) through a disk (blue). Appendix A 1 proves that the flux converges to zero as the disk radius r approaches zero.

The flux created by a small line element of the charged wire between $\boldsymbol{x}(s)$ and $\boldsymbol{x}(s+ds)$ is $(4\pi\varepsilon_0)^{-1}\Omega_r(\boldsymbol{x}(s))\nu(s)ds$, where $\Omega_r(\boldsymbol{x}(s))$ is the solid angle under which the disk is seen from the point $\boldsymbol{x}(s)$, see Fig. 6. Without loss of generality, we assume that $\nu(s)$ is positive. Then, the flux created by the charged wire is expressed as

$$\Phi_E = \int_{\text{disk}} \boldsymbol{E}\cdot d\boldsymbol{A} = \frac{1}{4\pi\varepsilon_0}\int_0^{s_{\max}} \Omega_r(\boldsymbol{x}(s))\nu(s)ds = \frac{1}{4\pi\varepsilon_0}\int_0^{z_{\max}} \Omega_r(\boldsymbol{x}(s(z)))\tilde{\nu}(z)dz. \tag{A5}$$

Here, $s_{\max}$ is the path length parameter value corresponding to the right end of the wire, $z_{\max} = z(s_{\max})$ is the corresponding z coordinate, and $s(z)$ is the inverse function of the parametrization component $z(s)$ which is assumed to be invertible. In the last step of Eq. (A5), we substituted the integration variable s by the z coordinate and, accordingly, we introduced the modified linear charge density $\tilde{\nu}(z) = \nu(s(z))\cdot\frac{ds}{dz} = \nu(s(z))\sqrt{1+(\frac{dx}{dz})^2+(\frac{dy}{dz})^2}$, which specifies the charge on the wire per unit distance along the z axis.

Now we give an upper bound to the flux by substituting the modified charge density by its maximum, $\tilde{\nu}_{\max}$:

$$\Phi_E \leqslant \Phi_E^{(1)} = \frac{\tilde{\nu}_{\max}}{4\pi\varepsilon_0}\int_0^{z_{\max}} \Omega_r(\boldsymbol{x}(s(z)))dz. \tag{A6}$$

We give a further, looser upper bound to the flux by utilizing the relation between the solid angles of the points of the wire and the points of the z axis, namely, $\Omega_r(\boldsymbol{x}(s(z))) \leqslant \Omega_r(0,0,z)$, see Fig. 6:

$$\Phi_E \leqslant \Phi_E^{(1)} \leqslant \Phi_E^{(2)} = \frac{\tilde{\nu}_{\max}}{4\pi\varepsilon_0}\int_0^{z_{\max}} \Omega_r(0,0,z)dz. \tag{A7}$$

Using $\Omega_r(0,0,z) = 2\pi\left(1 - \frac{z}{\sqrt{r^2+z^2}}\right)$ yields

$$\Phi_E^{(2)} = \frac{\tilde{\nu}_{\max}}{2\varepsilon_0}\int_0^{z_{\max}}\left(1 - \frac{z}{\sqrt{z^2+r^2}}\right)dz = \frac{\tilde{\nu}_{\max}}{2\varepsilon_0}\left(z_{\max} + r - \sqrt{z_{\max}^2 + r^2}\right) \tag{A8}$$

This upper bound $\Phi_E^{(2)}$ converges to zero as $r \to 0$, and hence the same is true for the flux Φ_E.

2. Second proof

To give an alternative proof of the charge density formula Eq. (7), we start with the electrostatic field created by a linear charge density,

$$\boldsymbol{E}(\boldsymbol{r}) = \frac{1}{4\pi\varepsilon_0}\int ds\ \nu(s)\frac{\boldsymbol{r} - \boldsymbol{r}(s)}{|\boldsymbol{r} - \boldsymbol{r}(s)|^3}, \tag{A9}$$

where $\boldsymbol{r}(s) = (0,0,s)$ is the parametrization of the line charge. For simplicity, we assume that the line charge is located along the z axis. We justify this assumption *a posteriori* by the fact that the contribution of the charge distribution far from the point in question to the surface integral vanishes in the $r \to 0$ limit. If the degeneracy line is smooth, in the $r \to 0$ limit it is locally well approximated by a straight line.

Substituting this into the integral for a cylinder surrounding the charge density,

$$\lim_{r\to 0}\int_0^{2\pi} d\vartheta \boldsymbol{E}(\boldsymbol{p}_r(s,\vartheta))\cdot[\partial_\vartheta \boldsymbol{p}_r \times \partial_s \boldsymbol{p}_r]_{s,\vartheta} = \lim_{r\to 0}\frac{1}{\varepsilon_0}\int ds'\ \nu(s')\frac{1}{2r\left[1 + \left(\frac{s-s'}{r}\right)^2\right]^{\frac{3}{2}}} = \frac{\nu(s)}{\varepsilon_0}, \tag{A10}$$

where $\boldsymbol{p}_r(\vartheta, s) = (r\cos\vartheta, r\sin\vartheta, s)$. In the last step, we used that the fraction in the integrand converges to $\delta(s - s')$ in the $r \to 0$ limit.

APPENDIX B: NUMERICAL TECHNIQUES TO OBTAIN THE FIGURES

In this Appendix, we outline the numerical techniques we used to obtain Figs. 3 and 4 of the main text.

1. Berry flux density—Figs. 3(a) and 4(a)

Figures 3(a) and 4(a) show the Berry flux density $\mathcal{B}_n$, defined via Eqs. (17) and (10), on the surface of the torus surrounding the circular degeneracy line. To obtain Fig. 3(a), our first step was to define a 300×300 square grid on the s, ϑ parameter space, and the corresponding grid of points on the torus, obtained via the parametrization $\boldsymbol{p}_r(s,\vartheta)$. The second step was to numerically approximate the derivatives in Eq. (10) on the grid points of the torus as

$$|\partial_{B_\alpha}\psi_0(\boldsymbol{B})\rangle \approx \frac{|\psi_0(\boldsymbol{B} + \delta\boldsymbol{e}_\alpha)\rangle - |\psi_0(\boldsymbol{B} - \delta\boldsymbol{e}_\alpha)\rangle}{2\delta}. \tag{B1}$$

Here, $\alpha \in \{x, y, z\}$, $\boldsymbol{e}_\alpha$ is the canonical unit vector pointing in direction α, and we used $\delta = 10^{-9}$. The gauge of the ground-state wave functions in the vicinity of a given $\boldsymbol{B}$ was fixed such that the greatest-magnitude component of the four-component wave function was chosen to be real and positive. Having the Berry curvature vector field $\boldsymbol{\mathcal{B}}$ at hand, our final step was to evaluate the Berry flux density by taking the normal projection in Eq. (17). The data shown in Fig. 4(a) is obtained similarly.

2. 2D Berry curvature—Figs. 3(b) and 4(b)

The 2D Berry curvature $\mathcal{B}_{2D}(s,\vartheta)$, plotted in Figs. 3(b) and 4(b), is defined in Eq. (12) of the main text. We claim that this 2D Berry curvature is related to the Berry flux density discussed in the previous section via

$$\mathcal{B}_{2D}(s,\vartheta) = r\left(1 + \frac{r}{R}\sin\vartheta\right)\mathcal{B}_n(\boldsymbol{p}_r(s,\vartheta)). \tag{B2}$$

Using this relation, we converted the data in Fig. 3(a) [Fig. 4(a)] to the data in Fig. 3(b) [Fig. 4(b)]. The proof of Eq. (B2) is straightforward: Eq. (20) is used at the right-hand side of Eq. (12), then Eq. (17) is used, and finally the absolute value $|\partial_\vartheta \boldsymbol{p}_r(s,\vartheta) \times \partial_s \boldsymbol{p}_r(s,\vartheta)|$ is evaluated using the specific parametrization in Eq. (18).

As a side remark, we also claim that the 2D Berry curvature can be expressed as

$$\mathcal{B}_{2D}(s,\vartheta) = -2\,\mathrm{Im}\,\langle\partial_\vartheta\tilde{\psi}_0|\partial_s\tilde{\psi}_0\rangle, \tag{B3}$$

where $\tilde{\psi}_0(s,\vartheta) = (\psi_0 \circ \boldsymbol{p}_r)(s,\vartheta)$. This is proven using the chain rule, which implies

$$\langle\partial_\vartheta\tilde{\psi}_0| = \sum_{\alpha\in\{x,y,z\}}(\partial_\vartheta p_{r,\alpha})\langle\partial_{B_\alpha}\psi_0|, \tag{B4}$$

$$|\partial_s\tilde{\psi}_0\rangle = \sum_{\beta\in\{x,y,z\}}(\partial_s p_{r,\beta})|\partial_{B_\beta}\psi_0\rangle. \tag{B5}$$

With these, we find

$$-2\,\mathrm{Im}\,\langle\partial_\vartheta\tilde{\psi}_0|\partial_s\tilde{\psi}_0\rangle = \sum_{\alpha,\beta\in\{x,y,z\}} -2\,\mathrm{Im}(\partial_\vartheta p_{r,\alpha})(\partial_s p_{r,\beta})\langle\partial_{B_\alpha}\psi_0|\partial_{B_\beta}\psi_0\rangle. \tag{B6}$$

Using Eq. (10), the right-hand side is transformed as

$$-2\,\mathrm{Im}\,\langle\partial_\vartheta\tilde{\psi}_0|\partial_s\tilde{\psi}_0\rangle = \sum_{\alpha,\beta\in\{x,y,z\}}(\partial_\vartheta p_{r,\alpha})(\partial_s p_{r,\beta})\epsilon_{\alpha\beta\gamma}\mathcal{B}_\gamma = [(\partial_\vartheta\boldsymbol{p}_r)\times(\partial_s\boldsymbol{p}_r)]\cdot\boldsymbol{\mathcal{B}}. \tag{B7}$$

This, together with Eq. (12), concludes the proof.

3. Apparent linear topological charge density—Figs. 3(c) and 4(c)

The apparent linear topological charge density $\tilde{\nu}_r(s)$ is defined in Eq. (13). To obtain the data shown in panels Fig. 3(c) and Fig. 4(c), we performed a numerical ϑ integration of $\mathcal{B}_{2D}(s,\vartheta)$, using an $N \times N$ grid in (s,ϑ) space,

$$\tilde{\nu}_r(s) = \frac{1}{2\pi}\int_0^{2\pi}\mathcal{B}_{2D}(s,\vartheta)d\vartheta \approx \frac{1}{N}\sum_{k=1}^{N}\mathcal{B}_{2D}\left(s, k\cdot\frac{2\pi}{N}\right), \tag{B8}$$

with $N = 300$ [$N = 1000$].

4. Chern number—Figs. 3(d) and 4(d)

The ground-state Chern number $\mathcal{Q}$ on the torus, as a function of the meridian radius r, is shown in Figs. 3(d) and 4(d). This quantity is obtained from the apparent topological charge density of panel c, via a numerical integration over the longitude path length s, following

$$\begin{aligned}\mathcal{Q}_r &= \frac{1}{2\pi}\int_S d\boldsymbol{A}\cdot\boldsymbol{\mathcal{B}} \\ &= \frac{1}{2\pi}\int_0^{2\pi R}\int_0^{2\pi}\mathcal{B}_{2\mathrm{D}}(s,\vartheta)d\vartheta ds \\ &= \int_0^{2\pi R}\tilde{\nu}_r(s)ds \approx \frac{2\pi R}{N}\sum_{k=1}^{N}\tilde{\nu}_r\left(k\cdot\frac{2\pi R}{N}\right). \end{aligned} \tag{B9}$$

APPENDIX C: JORDAN NORMAL FORMS FOR THE EXAMPLES IN THE MAIN TEXT

In this Appendix, we revisit the Jordan decomposition of 3×3 real matrices, and discuss the relation between the matrix $\hat{\boldsymbol{M}}$ introduced in Eq. (5) of the main text, its Jordan decomposition, and the magnetic degeneracy points.

In the main text, we have introduced the real valued nonsymmetric matrix $\hat{\boldsymbol{M}}$ in Eq. (5) as the central quantity of the two-spin problem. Also, we claimed that the directions of the degeneracy points in the magnetic-field parameter space are described by the left eigenvectors (left *ordinary eigenvectors*) of this matrix $\hat{\boldsymbol{M}}$. Because of the nonsymmetric property, $\hat{\boldsymbol{M}}$ is not always diagonalizable. Instead, it can be written as

$$\hat{\boldsymbol{M}} = \hat{\boldsymbol{p}}\hat{\boldsymbol{J}}\hat{\boldsymbol{p}}^{-1} = [\boldsymbol{w}_1 \quad \boldsymbol{w}_2 \quad \boldsymbol{w}_2]\hat{\boldsymbol{J}}\begin{bmatrix}\boldsymbol{v}_1^{\mathrm{T}}\\ \boldsymbol{v}_2^{\mathrm{T}}\\ \boldsymbol{v}_3^{\mathrm{T}}\end{bmatrix}, \tag{C1}$$

which is called the Jordan decomposition [58]. Here, $\hat{\boldsymbol{P}}^{-1}$ ($\hat{\boldsymbol{P}}$) is a nonsingular matrix whose rows (columns) are the left (right) *generalized eigenvectors* of $\hat{\boldsymbol{M}}$. From $\hat{\boldsymbol{P}}^{-1}\hat{\boldsymbol{P}} = \mathbb{1}$, it follows that $\boldsymbol{v}_i^{\mathrm{T}}\boldsymbol{w}_j = \delta_{ij}$. It is important to note that the left (right) generalized eigenvectors are not necessarily orthogonal to each other and not necessarily normalized. Also, the transformation matrix $\hat{\boldsymbol{P}}$ is not unique. The matrix $\hat{\boldsymbol{J}}$ is the Jordan normal form of $\hat{\boldsymbol{M}}$, which has a block-diagonal structure formed of Jordan blocks. In our case, Jordan blocks are matrices with the following structure:

$$\begin{aligned}\hat{\boldsymbol{J}}_{1\times1}(\lambda) &= (\lambda),\\ \hat{\boldsymbol{J}}_{2\times2}(\lambda) &= \begin{pmatrix}\lambda & 1\\ 0 & \lambda\end{pmatrix},\\ \hat{\boldsymbol{J}}_{3\times3}(\lambda) &= \begin{pmatrix}\lambda & 1 & 0\\ 0 & \lambda & 1\\ 0 & 0 & \lambda\end{pmatrix},\end{aligned} \tag{C2}$$

where the diagonal elements are filled with the eigenvalue λ and the superdiagonal is composed of ones.

A left generalized eigenvector of rank $m\in\{1,2,3\}$ corresponding to eigenvalue λ satisfies

$$\boldsymbol{v}^{\mathrm{T}}(\hat{\boldsymbol{M}}-\lambda\mathbb{1})^m = 0 \tag{C3}$$

and

$$\boldsymbol{v}^{\mathrm{T}}(\hat{\boldsymbol{M}}-\lambda\mathbb{1})^{m-1} \neq 0. \tag{C4}$$

The parallel condition in Eq. (4) is fulfilled by the left *ordinary eigenvectors* denoted as $\boldsymbol{b}$ which are the rank-1 generalized left eigenvectors. The ith row in $\hat{\boldsymbol{P}}^{-1}$ is an ordinary left eigenvector of $\hat{\boldsymbol{M}}$ if the ith row in $\hat{\boldsymbol{J}}$ does not contain a superdiagonal 1 element. Linear combinations of ordinary eigenvectors corresponding to the same eigenvalue are also ordinary eigenvectors.

In the following subsections, we provide the Jordan normal forms corresponding to the Hamiltonians and degeneracy patterns discussed in Secs. III A, III B, and IV. Note that in examples (II) and (V) discussed in the main text, we set both the interaction matrix $\hat{\boldsymbol{R}} = \mathbb{1}_{3\times3}$ and the right g tensor $\hat{\boldsymbol{g}}_{\mathrm{R}} = \mathbb{1}_{3\times3}$ as the 3×3 unit matrix, and hence the matrix $\hat{\boldsymbol{M}}$ equals the left g tensor $\hat{\boldsymbol{g}}_{\mathrm{L}}$.

1. Degeneracy pattern (II), Sec. III A

For the example Hamiltonian producing the degeneracy pattern (II), treated in Sec. III A, the left g tensor was specified in Eq. (15), leading to

$$\hat{\boldsymbol{M}}_{\mathrm{II}} = \hat{\boldsymbol{g}}_{\mathrm{L,II}}\hat{\boldsymbol{R}}_{\mathrm{II}}\hat{\boldsymbol{g}}_{\mathrm{R,II}}^{-1} = \hat{\boldsymbol{g}}_{\mathrm{L,II}} = \begin{pmatrix}2&0&0\\0&2&0\\0&1&4\end{pmatrix}. \tag{C5}$$

The matrices of the Jordan decomposition [see Eq. (C1)] of this matrix $\hat{\boldsymbol{M}}_{\mathrm{II}}$ read

$$\begin{aligned}\hat{\boldsymbol{J}}_{\mathrm{II}} &= \begin{pmatrix}4&0&0\\0&2&0\\0&0&2\end{pmatrix}, \quad \hat{\boldsymbol{P}}_{\mathrm{II}} = \frac{1}{2}\begin{pmatrix}0&0&2\\0&2&0\\1&-1&0\end{pmatrix},\\ \hat{\boldsymbol{P}}_{\mathrm{II}}^{-1} &= \begin{pmatrix}0&1&2\\0&1&0\\1&0&0\end{pmatrix}.\end{aligned} \tag{C6}$$

The Jordan normal form $\hat{\boldsymbol{J}}_{\mathrm{II}}$ is diagonal, it consists of three Jordan blocks: two blocks of the form $\hat{\boldsymbol{J}}_{1\times1}(2)$, and one block of the form $\hat{\boldsymbol{J}}_{1\times1}(4)$.

As seen from Eqs. (C1) and (C6), the left eigenvector corresponding to eigenvalue 4 is $\boldsymbol{v}_1 = (0,1,2)^T$. As claimed in Eq. (16), there are two magnetic Weyl points, forming a time-reversed pair, along the B-field direction set by $\boldsymbol{v}_1$. It is also seen in Eq. (C6) that two left eigenvectors corresponding to eigenvalue 2 are $\boldsymbol{v}_2 = (0,1,0)^T$ and $\boldsymbol{v}_3 = (1,0,0)^T$. In fact, all vectors in the subspace $\mathrm{Span}(\boldsymbol{v}_2,\boldsymbol{v}_3)$ are eigenvectors with eigenvalue 2. According to Eqs. (6) and (15), the corresponding magnetic degeneracy points form a circle with radius $R = 3/4$.

2. Degeneracy pattern (V), Sec. III B

In Sec. III B, describing the charged ellipse degeneracy pattern (V), the left g tensor and hence matrix $\hat{\boldsymbol{M}}$ was set to

$$\hat{\boldsymbol{M}}_{\mathrm{V}} = \begin{pmatrix}2&0&0\\0&2&0\\0&1&2\end{pmatrix}. \tag{C7}$$

A Jordan decomposition of this matrix is

$$\hat{\boldsymbol{J}}_{\mathrm{V}} = \begin{pmatrix} 2 & 1 & 0 \\ 0 & 2 & 0 \\ 0 & 0 & 2 \end{pmatrix}, \quad \hat{\boldsymbol{P}}_{\mathrm{V}} = \begin{pmatrix} 0 & 0 & 1 \\ 0 & 1 & 0 \\ 1 & 0 & 0 \end{pmatrix},$$
$$\hat{\boldsymbol{P}}_{\mathrm{V}}^{-1} = \begin{pmatrix} 0 & 0 & 1 \\ 0 & 1 & 0 \\ 1 & 0 & 0 \end{pmatrix}. \tag{C8}$$

The Jordan normal form $\hat{\boldsymbol{J}}_{\mathrm{V}}$ consists of the Jordan blocks $\hat{\boldsymbol{J}}_{1\times1}(2)$ and $\hat{\boldsymbol{J}}_{2\times2}(2)$. There is a superdiagonal 1 element in the first row, hence $\boldsymbol{v}_1 = (0, 0, 1)^{\mathrm{T}}$ is not an ordinary left eigenvector but a rank-2 generalized left eigenvector.

The ordinary eigenvectors are in the subspace $\mathrm{Span}(\boldsymbol{v}_2, \boldsymbol{v}_3)$, similarly to the previous case. As a consequence of this, and Eq. (6), the corresponding degeneracies are on a circle with radius $R = 3/4$ in the xy plane again. This is similar to the degeneracy circle of pattern (II), but there the circle was neutral while here it is charged.

Using Figs. 4(a)–4(c), we argued in the main text that the topological charge of this charged degeneracy circle is localized on two opposite points of the circle. Here we claim that the charge is located in the $\boldsymbol{v}_2$ direction. This can be illustrated by studying a parameter-dependent matrix $\hat{\boldsymbol{M}}$ that exemplifies a transition from the degeneracy pattern (II) formed by two equally charged Weyl points and a neutral circle to the degeneracy pattern (V) formed by the charged circle:

$$\hat{\boldsymbol{M}}_{\mathrm{II}\to\mathrm{V}}(\epsilon) = \begin{pmatrix} 2 & 0 & 0 \\ 0 & 2 & 0 \\ 0 & 1 & 2+\epsilon \end{pmatrix}. \tag{C9}$$

For $\epsilon > 0$, this matrix has a Jordan decomposition analogous to Eq. (C6), i.e., it implies the degeneracy pattern (II). In particular, its largest eigenvalue is $2+\epsilon$, with an ordinary left eigenvector $\boldsymbol{v}_1 = (0, 1, \epsilon)^{\mathrm{T}}$. As ϵ is tuned continuously to zero, then $\boldsymbol{v}_1$ coalesces with the (ϵ-independent) second left ordinary eigenvector $\boldsymbol{v}_2 = (0, 1, 0)^{\mathrm{T}}$. During this transition, the Weyl points approach the neutral ellipse and then merge with it at $\epsilon = 0$.

3. Degeneracy pattern (IV), Sec. IV

In Sec. IV, describing the charged ellipsoid degeneracy pattern (IV), the matrix $\hat{\boldsymbol{M}}$ was set to

$$\hat{\boldsymbol{M}}_{\mathrm{IV}} = 2 \cdot \mathbb{1}_{3\times3}. \tag{C10}$$

Every vector is an eigenvector, hence there are degeneracies in every direction. The distance of the degeneracy points from the origin is given by Eq. (6).

APPENDIX D: RANK OF THE EFFECTIVE g TENSOR IN THE POINTS OF THE DEGENERACY ELLIPSES

Figure 3 of the main text provides numerical evidence that the topological charge density of the neutral degeneracy ellipse, of pattern (II), is zero. Similarly, Fig. 4 shows that the topological charge density of the charged degeneracy ellipse, pattern (V), is concentrated at two charged points, whereas the linear charge density in all other points of the ellipse is zero. In this Appendix, we show that the above charge distributions are related to the ranks of the effective g tensors $\hat{\boldsymbol{g}}_{\mathrm{eff}}(\boldsymbol{B}_0)$ of the degeneracy points, defined in Eq. (30), namely, the effective g tensor is a rank-1 matrix for the charged points of the charged ellipse and a rank-2 matrix for the uncharged points of the charged ellipse and for every point of the neutral ellipse too. The rank-2 property implies a first-order energy splitting of the degeneracy as we leave the degenerate line in any perpendicular direction. In the case of a rank-1 effective g-tensor, there exists a direction perpendicular to the tangent vector of the degeneracy circle, with the property that the energy splitting is of higher-than-linear order if we leave the circle in that particular direction.

The effective g tensor for a ground-state degeneracy point at $\boldsymbol{B}_0 = B_0\boldsymbol{b}$ reads (Eq. (E11) of Ref. [11])

$$\hat{\boldsymbol{g}}_{\mathrm{eff}}(\boldsymbol{B}_0)\hat{\boldsymbol{O}} = \left(\frac{\hat{\boldsymbol{M}}+a^2}{1+a^2} - \frac{\hat{\boldsymbol{M}}-a}{\sqrt{1+a^2}}\right)\hat{\boldsymbol{g}}_{\mathrm{R}}\hat{\boldsymbol{R}}^{-1}\tilde{\boldsymbol{b}}\tilde{\boldsymbol{b}}^{\mathrm{T}} + \frac{\hat{\boldsymbol{M}}-a}{\sqrt{1+a^2}}\hat{\boldsymbol{g}}_{\mathrm{R}}\hat{\boldsymbol{R}}^{-1}, \tag{D1}$$

where

$$\tilde{\boldsymbol{b}} = \hat{\boldsymbol{R}}\hat{\boldsymbol{g}}_{\mathrm{R}}^{\mathrm{T}}\boldsymbol{b}/|\hat{\boldsymbol{g}}_{\mathrm{R}}^{\mathrm{T}}\boldsymbol{b}|. \tag{D2}$$

Note that, here, we use a slightly different notation, compared to that in Ref. [11]: Here we denote the dyadic product as a matrix product $\tilde{\boldsymbol{b}}\tilde{\boldsymbol{b}}^{\mathrm{T}}$ of a column vector and a row vector, instead of the alternative notation $\tilde{\boldsymbol{b}} \otimes \tilde{\boldsymbol{b}}$. The orthogonal matrix $\hat{\boldsymbol{O}}$, which is defined (see Eq. (C2) of Ref. [11]) as an (ambiguous) rotation fulfilling $\hat{\boldsymbol{O}}\tilde{\boldsymbol{b}} = \boldsymbol{e}_z$, e.g., the π rotation around the bisector of $\tilde{\boldsymbol{b}}$ and $\boldsymbol{e}_z$.

Equation (D1) for the effective g tensor is too complicated to determine $\mathrm{rank}[\hat{\boldsymbol{g}}_{\mathrm{eff}}(\boldsymbol{B}_0)]$ directly. Instead, in the forthcoming calculation, we show that the rank is reflected by the rank of a a simpler matrix $\hat{\boldsymbol{A}}_Q$, which we express below in Eq. (D17). Then, in Appendices D 1 and D 2, we use this matrix $\hat{\boldsymbol{A}}_Q$ to derive the rank of the effective g tensor on degeneracy ellipses.

As a first step in our calculation, we substitute $\tilde{\boldsymbol{b}}$ with $\boldsymbol{b}$ according to Eq. (D2), into Eq. (D1), and multiply the latter with $\hat{\boldsymbol{O}}^{-1}$ from the right:

$$\hat{\boldsymbol{g}}_{\mathrm{eff}}(\boldsymbol{b}) = \left[\left(\frac{\hat{\boldsymbol{M}}+a^2}{1+a^2} - \frac{\hat{\boldsymbol{M}}-a}{\sqrt{1+a^2}}\right)\frac{\hat{\boldsymbol{g}}_{\mathrm{R}}\hat{\boldsymbol{g}}_{\mathrm{R}}^{\mathrm{T}}\boldsymbol{b}\boldsymbol{b}^{\mathrm{T}}}{\boldsymbol{b}^{\mathrm{T}}\hat{\boldsymbol{g}}_{\mathrm{R}}\hat{\boldsymbol{g}}_{\mathrm{R}}^{\mathrm{T}}\boldsymbol{b}} + \frac{\hat{\boldsymbol{M}}-a}{\sqrt{1+a^2}}\right] \times \hat{\boldsymbol{g}}_{\mathrm{R}}\hat{\boldsymbol{R}}^{-1}\hat{\boldsymbol{O}}^{-1}. \tag{D3}$$

Here, we use $\boldsymbol{b}$ instead of $\boldsymbol{B}_0$ in the argument of $\hat{\boldsymbol{g}}_{\mathrm{eff}}$, because the latter quantity does not depend on the norm B_0.

In cases (II) and (V), where degeneracy ellipses appear, the directions of the magnetic degeneracy points are in the subspace of the second and third left generalized eigenvectors. That is, the degeneracy points can be parameterized by the angle $\varphi \in [0, 2\pi[$ via

$$\boldsymbol{b} = \beta_2\boldsymbol{v}_2 + \beta_3\boldsymbol{v}_3 = \beta(\boldsymbol{v}_2\cos\varphi + \boldsymbol{v}_3\sin\varphi), \tag{D4}$$

with $\beta = \sqrt{\beta_2^2+\beta_3^2}$. Since $\boldsymbol{v}_2$ and $\boldsymbol{v}_3$ are not necessarily orthogonal and normalized, β is not necessarily $|\boldsymbol{b}|$ and φ is not necessarily the angle between $\boldsymbol{b}$ and $\boldsymbol{v}_2$.

The forthcoming steps lack an *a priori* intuitive justification, but *a posteriori* they prove to be particularly useful. First,

let us recall that according to Eq. (C1), the left generalized eigenvectors form the rows in the similarity transformation matrix $\hat{\boldsymbol{P}}^{-1}$ in the Jordan decomposition of $\hat{\boldsymbol{M}}$. Using this, $\boldsymbol{b}^{\mathrm{T}}$ can be written as the second row of the matrix $\hat{\boldsymbol{Q}}\hat{\boldsymbol{P}}^{-1}$, that is,

$$\boldsymbol{b}^{\mathrm{T}} = (\hat{\boldsymbol{Q}}\hat{\boldsymbol{P}}^{-1})_{2,.}, \tag{D5}$$

where

$$\hat{\boldsymbol{Q}} = \beta \begin{pmatrix} 1 & 0 & 0 \\ 0 & \cos\varphi & \sin\varphi \\ 0 & -\sin\varphi & \cos\varphi \end{pmatrix}. \tag{D6}$$

Inserting a unit matrix in the form of $\hat{\boldsymbol{P}}^{-1}\hat{\boldsymbol{P}}$ to Eq. (D5) yields

$$\boldsymbol{b}^{\mathrm{T}} = (\hat{\boldsymbol{P}}^{-1}\hat{\boldsymbol{P}}\hat{\boldsymbol{Q}}\hat{\boldsymbol{P}}^{-1})_{2,.} \equiv (\hat{\boldsymbol{P}}^{-1}\hat{\boldsymbol{Q}}')_{2,.} = \boldsymbol{v}_2^{\mathrm{T}}\hat{\boldsymbol{Q}}'. \tag{D7}$$

Here the sign $\equiv$ denotes the definition of $\hat{\boldsymbol{Q}}'$ and in the last step, we used Eq. (C1).

Substituting Eq. (D7) to the effective g-tensor of Eq. (D3), we obtain

$$\hat{\boldsymbol{g}}_{\mathrm{eff}}(\hat{\boldsymbol{Q}}'^{\mathrm{T}}\boldsymbol{v}_2) = \left[\left(\frac{\hat{\boldsymbol{M}}+a^2}{1+a^2} - \frac{\hat{\boldsymbol{M}}-a}{\sqrt{1+a^2}}\right)\hat{\boldsymbol{D}} + \frac{\hat{\boldsymbol{M}}-a}{\sqrt{1+a^2}}\right] \times \hat{\boldsymbol{g}}_{\mathrm{R}}\hat{\boldsymbol{R}}^{-1}\hat{\boldsymbol{O}}^{-1}, \tag{D8}$$

where we introduced the shorthand

$$\hat{\boldsymbol{D}} = \frac{\hat{\boldsymbol{g}}_{\mathrm{R}}\hat{\boldsymbol{g}}_{\mathrm{R}}^{\mathrm{T}}\hat{\boldsymbol{Q}}'^{\mathrm{T}}\boldsymbol{v}_2\boldsymbol{v}_2^{\mathrm{T}}\hat{\boldsymbol{Q}}'}{\boldsymbol{v}_2^{\mathrm{T}}\hat{\boldsymbol{Q}}'\hat{\boldsymbol{g}}_{\mathrm{R}}\hat{\boldsymbol{g}}_{\mathrm{R}}^{\mathrm{T}}\hat{\boldsymbol{Q}}'^{\mathrm{T}}\boldsymbol{v}_2}, \tag{D9}$$

which is a dyadic product.

Next, we further transform $\hat{\boldsymbol{M}}$ and $\hat{\boldsymbol{D}}$ in Eq. (D8), starting with the latter. Substituting unit matrices into Eq. (D9) yields

$$\hat{\boldsymbol{D}} = \frac{(\hat{\boldsymbol{Q}}'^{-1}\hat{\boldsymbol{P}}\hat{\boldsymbol{P}}^{-1}\hat{\boldsymbol{Q}}')\hat{\boldsymbol{g}}_{\mathrm{R}}\hat{\boldsymbol{g}}_{\mathrm{R}}^{\mathrm{T}}\hat{\boldsymbol{Q}}'^{\mathrm{T}}\boldsymbol{v}_2\boldsymbol{v}_2^{\mathrm{T}}\hat{\boldsymbol{Q}}'}{\boldsymbol{v}_2^{\mathrm{T}}(\hat{\boldsymbol{P}}\hat{\boldsymbol{P}}^{-1})\hat{\boldsymbol{Q}}'\hat{\boldsymbol{g}}_{\mathrm{R}}\hat{\boldsymbol{g}}_{\mathrm{R}}^{\mathrm{T}}\hat{\boldsymbol{Q}}'^{\mathrm{T}}\boldsymbol{v}_2}. \tag{D10}$$

Then, using the associative nature of matrix multiplication, we obtain

$$\hat{\boldsymbol{D}} = \frac{\hat{\boldsymbol{Q}}'^{-1}\hat{\boldsymbol{P}}(\hat{\boldsymbol{P}}^{-1}\hat{\boldsymbol{Q}}'\hat{\boldsymbol{g}}_{\mathrm{R}}\hat{\boldsymbol{g}}_{\mathrm{R}}^{\mathrm{T}}\hat{\boldsymbol{Q}}'^{\mathrm{T}}\boldsymbol{v}_2)\boldsymbol{v}_2^{\mathrm{T}}\hat{\boldsymbol{Q}}'}{\boldsymbol{v}_2^{\mathrm{T}}\hat{\boldsymbol{P}}(\hat{\boldsymbol{P}}^{-1}\hat{\boldsymbol{Q}}'\hat{\boldsymbol{g}}_{\mathrm{R}}\hat{\boldsymbol{g}}_{\mathrm{R}}^{\mathrm{T}}\hat{\boldsymbol{Q}}'^{\mathrm{T}}\boldsymbol{v}_2)} = \frac{\hat{\boldsymbol{Q}}'^{-1}\hat{\boldsymbol{P}}\boldsymbol{r}\boldsymbol{v}_2^{\mathrm{T}}\hat{\boldsymbol{Q}}'}{\boldsymbol{v}_2^{\mathrm{T}}\hat{\boldsymbol{P}}\boldsymbol{r}}, \tag{D11}$$

where we introduced

$$\boldsymbol{r} = \hat{\boldsymbol{P}}^{-1}\hat{\boldsymbol{Q}}'\hat{\boldsymbol{g}}_{\mathrm{R}}\hat{\boldsymbol{g}}_{\mathrm{R}}^{\mathrm{T}}\hat{\boldsymbol{Q}}'^{\mathrm{T}}\boldsymbol{v}_2. \tag{D12}$$

Then, we substitute the definition of $\hat{\boldsymbol{Q}}'$ from Eq. (D7) to Eq. (D11), yielding

$$\hat{\boldsymbol{D}} = \frac{\hat{\boldsymbol{P}}\hat{\boldsymbol{Q}}^{-1}\hat{\boldsymbol{P}}^{-1}\hat{\boldsymbol{P}}\boldsymbol{r}\boldsymbol{v}_2^{\mathrm{T}}\hat{\boldsymbol{P}}\hat{\boldsymbol{Q}}\hat{\boldsymbol{P}}^{-1}}{\boldsymbol{v}_2^{\mathrm{T}}\hat{\boldsymbol{P}}\boldsymbol{r}} = \hat{\boldsymbol{P}}\hat{\boldsymbol{Q}}^{-1}\frac{\boldsymbol{r}}{r_2}(0 \quad 1 \quad 0)\hat{\boldsymbol{Q}}\hat{\boldsymbol{P}}^{-1}. \tag{D13}$$

The denominator r_2, which is the second vector component of $\boldsymbol{r}$, appears from the scalar product of $\boldsymbol{r}$ with $\boldsymbol{v}_2^{\mathrm{T}}\hat{\boldsymbol{P}} \equiv (0\ 1\ 0)$. Note that $r_2 = |\hat{\boldsymbol{g}}_{\mathrm{R}}^{\mathrm{T}}\boldsymbol{b}|^2$, which follows, e.g., from Eqs. (D12) and (D7), and it guarantees that the denominator in Eq. (D13) is nonzero.

According to Eq. (D13), the matrix $\hat{\boldsymbol{D}}$ can be thought of as a result of a similarity transformation generated by $\hat{\boldsymbol{P}}\hat{\boldsymbol{Q}}^{-1}$. Now, we transform the terms of Eq. (D8) containing $\hat{\boldsymbol{M}}$ to a similar form. Multiplying $\hat{\boldsymbol{M}}$ with appropriately composed unit matrices, using its Jordan decomposition, and introducing the *transformed Jordan normal form* via

$$\hat{\boldsymbol{J}}_Q = \hat{\boldsymbol{Q}}\hat{\boldsymbol{J}}\hat{\boldsymbol{Q}}^{-1}, \tag{D14}$$

we find

$$\hat{\boldsymbol{M}} = (\hat{\boldsymbol{P}}\hat{\boldsymbol{Q}}^{-1}\hat{\boldsymbol{Q}}\hat{\boldsymbol{P}}^{-1})(\hat{\boldsymbol{P}}\hat{\boldsymbol{J}}\hat{\boldsymbol{P}}^{-1})(\hat{\boldsymbol{P}}\hat{\boldsymbol{Q}}^{-1}\hat{\boldsymbol{Q}}\hat{\boldsymbol{P}}^{-1}) = \hat{\boldsymbol{P}}\hat{\boldsymbol{Q}}^{-1}\hat{\boldsymbol{J}}_Q\hat{\boldsymbol{Q}}\hat{\boldsymbol{P}}^{-1}. \tag{D15}$$

Inserting Eqs. (D13) and (D15) into Eq. (D8), we find the following expression for the effective g tensor:

$$\hat{\boldsymbol{g}}_{\mathrm{eff}}(\boldsymbol{b}) = \hat{\boldsymbol{P}}\hat{\boldsymbol{Q}}^{-1}\hat{\boldsymbol{A}}_Q\hat{\boldsymbol{Q}}\hat{\boldsymbol{P}}^{-1}\hat{\boldsymbol{g}}_{\mathrm{R}}\hat{\boldsymbol{R}}^{-1}\hat{\boldsymbol{O}}^{-1}, \tag{D16}$$

where we introduced

$$\hat{\boldsymbol{A}}_Q = \left(\frac{\hat{\boldsymbol{J}}_Q+a^2}{1+a^2} - \frac{\hat{\boldsymbol{J}}_Q-a}{\sqrt{1+a^2}}\right)\frac{\boldsymbol{r}}{r_2}(0 \quad 1 \quad 0) + \frac{\hat{\boldsymbol{J}}_Q-a}{\sqrt{1+a^2}}. \tag{D17}$$

Matrix $\hat{\boldsymbol{A}}_Q$ has the same rank as the effective g tensor because they only differ by multiplications of nonsingular matrices. In what follows, we will determine the rank of the g tensor at the points of the degeneracy ellipses by determining the rank of $\hat{\boldsymbol{A}}_Q$.

1. Neutral ellipse

In Eq. (C6), we have shown an example Jordan decomposition corresponding to a degeneracy pattern including a neutral ellipse. More generally, the normal form of that degeneracy pattern has a twofold degeneracy of the following kind (see Table I of Ref. [11]):

$$\hat{\boldsymbol{J}}_{\mathrm{II}} = \begin{pmatrix} b & 0 & 0 \\ 0 & a & 0 \\ 0 & 0 & a \end{pmatrix}, \tag{D18}$$

where $a, b > 0$ and $a \neq b$. Since its second Jordan block is proportional to the 2×2 unit matrix, the transformation with $\hat{\boldsymbol{Q}}$ defined in Eq. (D6) leaves the normal form invariant,

$$\hat{\boldsymbol{J}}_{Q,\mathrm{II}} = \hat{\boldsymbol{J}}_{\mathrm{II}}, \tag{D19}$$

for every φ. That means that every point of a neutral ellipse has the same rank effective g tensor. Then, expressing $\hat{\boldsymbol{A}}_Q$ from Eqs. (D17), (D19), and (D18) yields

$$\begin{aligned}\hat{\boldsymbol{A}}_Q &= \begin{pmatrix} \frac{b+a^2}{1+a^2} - \frac{b-a}{\sqrt{1+a^2}} & 0 & 0 \\ 0 & \frac{a+a^2}{1+a^2} & 0 \\ 0 & 0 & \frac{a+a^2}{1+a^2} \end{pmatrix}\begin{pmatrix} r_1/r_2 \\ 1 \\ r_3/r_2 \end{pmatrix}(0 \quad 1 \quad 0) \\ &\quad + \begin{pmatrix} \frac{b-a}{\sqrt{1+a^2}} & 0 & 0 \\ 0 & 0 & 0 \\ 0 & 0 & 0 \end{pmatrix} \\ &= \begin{pmatrix} \frac{b-a}{\sqrt{1+a^2}} & \left[\frac{b+a^2}{1+a^2} - \frac{b-a}{\sqrt{1+a^2}}\right]\frac{r_1}{r_2} & 0 \\ 0 & \frac{a(1+a)}{1+a^2} & 0 \\ 0 & \frac{a(1+a)}{1+a^2}\frac{r_3}{r_2} & 0 \end{pmatrix}. \end{aligned} \tag{D20}$$

$\hat{\boldsymbol{A}}_Q$ cannot be a dyadic product because the condition $A_{Q,11}A_{Q,22} = A_{Q,12}A_{Q,21}$ cannot be satisfied as $A_{Q,11}, A_{Q,22} \neq 0$

and $A_{Q,21} = 0$. That means $\mathrm{rank}(\hat{\boldsymbol{g}}_{\mathrm{eff}}) > 1$. The determinant of the effective g tensor is zero [Eq. (E23) of Ref. [11] with $c = a$], therefore $\mathrm{rank}(\hat{\boldsymbol{g}}_{\mathrm{eff}}) < 3$. This way, we proved that the rank is 2 for every points of the neutral degeneracy ellipse.

2. Charged ellipse

In Eq. (C8), we have shown an example for a Jordan decomposition corresponding to a degeneracy pattern of a charged ellipse. More generally, the Jordan normal form of that degeneracy pattern has a threefold eigenvalue degeneracy and a single 1 element in the superdiagonal,

$$\hat{\boldsymbol{J}}_{\mathrm{V}} = \begin{pmatrix} a & 1 & 0 \\ 0 & a & 0 \\ 0 & 0 & a \end{pmatrix}, \tag{D21}$$

with $a > 0$. Now $\hat{\boldsymbol{J}}_{Q,\mathrm{V}}$ does depend on the angle φ parametrizing the degeneracy point along the degeneracy ellipse:

$$\hat{\boldsymbol{J}}_{Q,\mathrm{V}} = \begin{pmatrix} a & \cos\varphi & -\sin\varphi \\ 0 & a & 0 \\ 0 & 0 & a \end{pmatrix}. \tag{D22}$$

Expressing $\hat{\boldsymbol{A}}_Q$ from Eqs. (D17) and (D22) yields

$$\begin{aligned} \hat{\boldsymbol{A}}_Q &= \begin{pmatrix} \frac{a+a^2}{1+a^2} & \cos\varphi\left[\frac{1}{1+a^2} - \frac{1}{\sqrt{1+a^2}}\right] & -\sin\varphi\left[\frac{1}{1+a^2} - \frac{1}{\sqrt{1+a^2}}\right] \\ 0 & \frac{a+a^2}{1+a^2} & 0 \\ 0 & 0 & \frac{a+a^2}{1+a^2} \end{pmatrix} \begin{pmatrix} r_1/r_2 \\ 1 \\ r_3/r_2 \end{pmatrix} (0 \quad 1 \quad 0) + \begin{pmatrix} 0 & \frac{\cos\varphi}{\sqrt{1+a^2}} & \frac{-\sin\varphi}{\sqrt{1+a^2}} \\ 0 & 0 & 0 \\ 0 & 0 & 0 \end{pmatrix} \\ &= \begin{pmatrix} 0 & A_{Q,12} & -\frac{\sin(\varphi)}{\sqrt{1+a^2}} \\ 0 & \frac{a(1+a)}{1+a^2} & 0 \\ 0 & A_{Q,32} & 0 \end{pmatrix}, \end{aligned} \tag{D23}$$

where the elements $A_{Q,12}$ and $A_{Q,32}$ are given by lengthy but unimportant expressions. Similarly to the neutral ellipse, the condition $A_{Q,12}A_{Q,23} = A_{Q,13}A_{Q,22}$ is not satisfied for $\sin\varphi \neq 0$, hence the rank of the effective g-tensor is 2 for those points. However, if $\sin\varphi = 0$, i.e., if the magnetic field is along the direction of $\boldsymbol{v}_2$, the matrix $\hat{\boldsymbol{A}}$ is clearly a dyadic product and not a zero matrix, hence its rank is 1, implying that the rank of the effective g tensor is also 1.

Finally, let us consider this latter case, when the rank of the effective g tensor is 1. Starting at the degeneracy point $\boldsymbol{B}_0$, and changing the magnetic field by $\delta\boldsymbol{B}$ along the degeneracy line as $\boldsymbol{B} = \boldsymbol{B}_0 + \delta\boldsymbol{B}$, the energy splitting induced by $\delta\boldsymbol{B}$ is at least of second order in $\delta\boldsymbol{B}$. Since the rank of the effective g tensor is 1, there must be a plane of higher-order splitting, that is, a plane along which the energy splitting is at least of second order in $\delta\boldsymbol{B}$. Which is the second direction, which spans this plane together with the direction of the degeneracy ellipse?

This question can be answered by recasting the rank-1 effective g tensor as a dyadic product of two vectors. Without the derivation, we claim that one way this can be done is as follows:

$$\hat{\boldsymbol{g}}_{\mathrm{eff}}(\boldsymbol{v}_2) = \boldsymbol{d}_1\boldsymbol{d}_2^{\mathrm{T}}, \tag{D24}$$

where

$$\boldsymbol{d}_1 = \frac{1}{1+a^2}\left[a(1+a)\frac{\hat{\boldsymbol{g}}_{\mathrm{R}}\hat{\boldsymbol{g}}_{\mathrm{R}}^{\mathrm{T}}\boldsymbol{v}_2}{\boldsymbol{v}_2^{\mathrm{T}}\hat{\boldsymbol{g}}_{\mathrm{R}}\hat{\boldsymbol{g}}_{\mathrm{R}}^{\mathrm{T}}\boldsymbol{v}_2} + \boldsymbol{w}_1\right], \quad \boldsymbol{d}_2 = \hat{\boldsymbol{O}}\hat{\boldsymbol{R}}\hat{\boldsymbol{g}}_{\mathrm{R}}^{\mathrm{T}}\boldsymbol{v}_2, \tag{D25}$$

where $\boldsymbol{w}_1$ is the right generalized eigenvector defined in Eq. (C1). The column vector $\boldsymbol{d}_1$ in the square bracket defines the direction of maximal linear splitting in $\delta\boldsymbol{B}$, cf. Eq. (30). If $\delta\boldsymbol{B}$ lies in the plane perpendicular to that vector, then the energy splitting is at least second order in $\delta\boldsymbol{B}$.

APPENDIX E: RANK-2 POINTS OF A DEGENERACY LINE CARRY ZERO LINEAR TOPOLOGICAL CHARGE DENSITY

In this Appendix, we show that, in general, degeneracy lines consisting of rank-2 points carry zero linear topological charge density. For simplicity, we assume that the degeneracy line is along the B_z axis.

We use $x \equiv B_x$, $y \equiv B_y$, and $z \equiv B_z$ for brevity, and we shift the coordinate system of the magnetic parameter space such that the rank-2 point we consider is in the origin, where $(x, y, z) = 0$. From now on, we further simplify notation by using $\psi_0(s, \vartheta)$ instead of $\tilde{\psi}_0(s, \vartheta)$ [cf. Eq. (B3)].

According to Eq. (13), our goal is to evaluate

$$\begin{aligned} \nu(0) &= \frac{1}{2\pi}\lim_{r\to 0}\int_0^{2\pi} d\vartheta\, \mathcal{B}_{2\mathrm{D}}(s, \vartheta) \\ &= \frac{1}{2\pi}\lim_{r\to 0}\int_0^{2\pi} d\vartheta\,(-2)\,\mathrm{Im}\,[\langle\partial_\vartheta\psi_0|\partial_s\psi_0\rangle]. \end{aligned} \tag{E1}$$

For the parameter-space geometry we consider, the relation between the Cartesian coordinates and the torus parameters is $x = r\cos\vartheta$, $y = r\sin\vartheta$, and $s = z$. Our strategy is to evaluate the above ϑ integral, i.e., to show that it vanishes, by using an approximate ground state ψ_0 for $r \to 0$, obtained via a z-dependent two-level effective Hamiltonian.

Along the z axis, in the small neighborhood of the degeneracy point, we take an orthonormal basis $(\eta(z), \chi(z))$ of the degenerate ground-state subspace for each z, such that the two basis states depend on z continuously. Using this basis, we define the effective Hamiltonian of the degeneracy point $(0, 0, z)$ as follows:

$$H_{\mathrm{eff}}(z) = P(z)H(x, y, z)P(z), \tag{E2}$$

where $P(z) = |\eta(z)\rangle\langle\eta(z)| + |\chi(z)\rangle\langle\chi(z)|$ projects on the two-dimensional ground-state subspace (this projector P should not be confused by the similarity transformation $\hat{\boldsymbol{P}}$).

This effective Hamiltonian can also be written as

$$H_{\text{eff}}(z) = \boldsymbol{x} \cdot \hat{\boldsymbol{g}}_{2\times 3}(z)\boldsymbol{\tau}(z), \tag{E3}$$

where $\boldsymbol{x} = (x, y)^{\mathrm{T}}$ and $\boldsymbol{\tau} = (\tau_x, \tau_y, \tau_z)^{\mathrm{T}}$ are the Pauli operators acting on the states $(\eta(z), \chi(z))$, e.g., $\tau(z) = \frac{1}{2}(|\eta(z)\rangle\langle\eta(z)| - |\chi(z)\rangle\langle\eta(z)|)$. Furthermore, $\hat{\boldsymbol{g}}_{2\times 3}$ is a 2×3 matrix of the form

$$\hat{\boldsymbol{g}}_{2\times 3} = \begin{pmatrix} g_{xx} & g_{xy} & g_{xz} \\ g_{yx} & g_{yy} & g_{yz} \end{pmatrix}. \tag{E4}$$

The coordinate z is absent from Eq. (E3), since our degeneracy point is on a degeneracy line of direction z, i.e., the two energy levels of the Hamiltonian must be degenerate as we move along the z axis.

The matrix $\hat{\boldsymbol{g}}_{2\times 3}(z)$ is of size 2×3 and of rank 2, hence it can be further simplified to a block matrix with a nonzero 2×2 block and a vanishing 2×1 block [see Eq. (E9) below], using a z-dependent unitary transformation of the basis $(|\eta(z)\rangle, |\chi(z)\rangle)$. To this end, we introduce the vectors $\boldsymbol{g}_x = (g_{xx}, g_{xy}, g_{xz})^{\mathrm{T}}$ and $\boldsymbol{g}_y = (g_{yx}, g_{yy}, g_{yz})^{\mathrm{T}}$, which are linearly independent because of the rank. We further introduce the vector

$$\boldsymbol{g}_\perp(z) = \boldsymbol{g}_x(z) \times \boldsymbol{g}_y(z), \tag{E5}$$

for which it holds that

$$\hat{\boldsymbol{g}}_{2\times 3}\boldsymbol{g}_\perp = 0. \tag{E6}$$

Now we introduce the orthogonal matrix $\hat{\boldsymbol{O}}(z)$ which rotates $\boldsymbol{g}_\perp(z)$ to the z direction,

$$\hat{\boldsymbol{O}}\boldsymbol{g}_\perp = g\boldsymbol{e}_z, \tag{E7}$$

with $g(z) = |\boldsymbol{g}_\perp(z)|$. One possible choice for $\hat{\boldsymbol{O}}(z)$ is an orthogonal matrix which rotates 180° around the bisector $\boldsymbol{t}(z)$ of $\boldsymbol{e}_z$ and $\boldsymbol{g}_\perp(z)$. Now we substitute the identity $\hat{\boldsymbol{O}}^{-1}\hat{\boldsymbol{O}}$ into Eq. (E6) to obtain

$$\hat{\boldsymbol{g}}_{2\times 3}\boldsymbol{g}_\perp = (\hat{\boldsymbol{g}}_{2\times 3}\hat{\boldsymbol{O}}^{-1})(\hat{\boldsymbol{O}}\boldsymbol{g}_\perp) = \hat{\boldsymbol{g}}'_{2\times 3}g\boldsymbol{e}_z = 0, \tag{E8}$$

where we introduced $\hat{\boldsymbol{g}}'_{2\times 3}(z) = \hat{\boldsymbol{g}}_{2\times 3}(z)\hat{\boldsymbol{O}}^{-1}(z)$, which has the form

$$\hat{\boldsymbol{g}}'_{2\times 3} = \begin{pmatrix} g'_{xx} & g'_{xy} & 0 \\ g'_{yx} & g'_{yy} & 0 \end{pmatrix}. \tag{E9}$$

After these steps, we finally simplify the effective Hamiltonian defined in Eq. (E3) with a unitary transformation. Substituting $\hat{\boldsymbol{O}}^{-1}\hat{\boldsymbol{O}}$ yields

$$H_{\text{eff}}(z) = \boldsymbol{x} \cdot \hat{\boldsymbol{g}}_{2\times 3}(z)\hat{\boldsymbol{O}}^{-1}(z)\hat{\boldsymbol{O}}(z)\boldsymbol{\tau}(z) = \boldsymbol{x} \cdot \hat{\boldsymbol{g}}'_{2\times 3}(z)\boldsymbol{\tau}'(z), \tag{E10}$$

where the new Pauli operator reads

$$\boldsymbol{\tau}'(z) = \hat{\boldsymbol{O}}(z)\boldsymbol{\tau}(z) = U(z)\boldsymbol{\tau}(z)U^\dagger(z). \tag{E11}$$

After the first equation sign, $\hat{\boldsymbol{O}}$ transforms the vector components of $\boldsymbol{\tau}$, while after the second equation sign, the corresponding unitary matrix $U(z) = \exp(-i\pi\boldsymbol{t}(z) \cdot \boldsymbol{\tau}(z)) = -i\boldsymbol{t}(z) \cdot \boldsymbol{\tau}(z)$ transforms the operators in the Hilbert space. In Eq. (E10), the Pauli operator τ'_z does not appear, thus we can simplify the effective Hamiltonian by introducing the 2×2 nonzero block $\hat{\boldsymbol{g}}_{2\times 2}$ of the matrix $\hat{\boldsymbol{g}}'_{2\times 3}$ in Eq. (E9), and the two-component vector operator $\boldsymbol{\tau}_2 = (\tau'_x, \tau'_y)^{\mathrm{T}}$, yielding

$$H_{\text{eff}}(z) = \boldsymbol{x} \cdot \hat{\boldsymbol{g}}_{2\times 2}(z)\boldsymbol{\tau}_2(z). \tag{E12}$$

This two-level effective Hamiltonian is straightforward to diagonalize, and its diagonalization provides a formula for the unique ground state away from the z axis,

$$|\psi_0(s, \vartheta)\rangle \equiv |\psi_0(z, \vartheta)\rangle \approx \frac{1}{\sqrt{2}}\left(|\eta'(z)\rangle - e^{i\alpha(z,\vartheta)}|\chi'(z)\rangle\right), \tag{E13}$$

where

$$|\nu'(z)\rangle = U(z)|\nu(z)\rangle, \tag{E14}$$

$$|\chi'(z)\rangle = U(z)|\chi(z)\rangle \tag{E15}$$

are the transformed basis states and $\alpha(z, \vartheta)$ is the polar angle of the vector $\hat{\boldsymbol{g}}^{\mathrm{T}}_{2\times 2}\boldsymbol{x}$. A key property of this angle is

$$\alpha(z, \vartheta + \pi) = \alpha(z, \vartheta) + \pi. \tag{E16}$$

As we show below, this property implies $\mathcal{B}_{2\mathrm{D}}(s, \vartheta) = -\mathcal{B}_{2\mathrm{D}}(s, \vartheta + \pi)$, and hence a vanishing result of the integral in Eq. (E1).

To compute the integrand of Eq. (E1), we first evaluate the derivatives of the ground state Eq. (E13):

$$|\partial_\vartheta \psi_0\rangle = \frac{-i}{\sqrt{2}}(\partial_\vartheta\alpha)e^{i\alpha}|\chi'\rangle, \tag{E17}$$

$$|\partial_z \psi_0\rangle = \frac{1}{\sqrt{2}}(|\partial_z\eta'\rangle - e^{i\alpha}|\partial_z\chi'\rangle - i(\partial_z\alpha)e^{i\alpha}|\chi'\rangle). \tag{E18}$$

Then, the scalar product in the integrand of Eq. (E1) reads

$$\begin{aligned}\langle\partial_\vartheta\psi_0|\partial_z\psi_0\rangle = \tfrac{1}{2}[&i(\partial_\vartheta\alpha)e^{-i\alpha}\langle\chi'|\partial_z\eta'\rangle + i(\partial_\vartheta\alpha)\langle\chi'|\partial_z\chi'\rangle \\ &+ (\partial_\vartheta\alpha)(\partial_z\alpha)].\end{aligned} \tag{E19}$$

The second term in the square bracket is real, since

$$\mathrm{Re}\langle\chi'|\partial_z\chi'\rangle = \tfrac{1}{2}(\langle\chi'|\partial_z\chi'\rangle + \langle\partial_z\chi'|\chi'\rangle) = \tfrac{1}{2}\partial_z\langle\chi'|\chi'\rangle = 0. \tag{E20}$$

Furthermore, the third term is also real, since α, defined as an angle, is real valued.

As a consequence, the imaginary part of the scalar product in the integrand of Eq. (E1) reads

$$\mathrm{Im}\,\langle\partial_\vartheta\psi_0|\partial_z\psi_0\rangle = \tfrac{1}{4}[(\partial_\vartheta\alpha)e^{-i\alpha}\langle\chi'|\partial_z\eta'\rangle + \text{c.c.}]. \tag{E21}$$

From this result, using Eq. (E16), it follows that

$$\begin{aligned}&\mathrm{Im}\,\langle\partial_\vartheta\psi_0(z, \vartheta + \pi)|\partial_z\psi_0(z, \vartheta + \pi)\rangle \\ &\quad = -\,\mathrm{Im}\,\langle\partial_\vartheta\psi_0(z, \vartheta)|\partial_z\psi_0(z, \vartheta)\rangle.\end{aligned} \tag{E22}$$

Finally, Eq. (E22) implies that the ϑ integral of Eq. (E1) vanishes.

While the topological charge density vanishes at rank-2 points of a degeneracy line, the Berry curvature, even at an isolated degeneracy line, is not identically zero. To see this, we consider a small disk D intersecting the degeneracy line and calculate the integral of the Berry connection $\boldsymbol{\mathcal{A}} = i\langle\psi_0|\boldsymbol{\nabla}\psi_0\rangle$ around the perimeter of the disk, which is a loop surrounding

the line degeneracy:

$$\oint_{\partial D} \boldsymbol{\mathcal{A}} \cdot d\boldsymbol{l} = i \int_0^{2\pi} \langle \psi_0 | \partial_\vartheta \psi_0 \rangle d\vartheta = \frac{1}{2} \int_0^{2\pi} \partial_\vartheta \alpha(z, \vartheta) d\vartheta = \frac{1}{2}[\alpha(z, 2\pi) - \alpha(z, 0)] = \pi. \tag{E23}$$

This result is independent of the radius of the disk chosen.

If the degeneracy is broken by some perturbation, the Berry curvature becomes well-defined and finite everywhere, with a large Berry curvature along the position of the degeneracy line. In this case, the integral of the Berry curvature for the disk equals the integral of the Berry connection around the perimeter:

$$\iint_D \boldsymbol{\mathcal{B}} \cdot d\boldsymbol{A} = \oint_{\partial D} \boldsymbol{\mathcal{A}} \cdot d\boldsymbol{l}. \tag{E24}$$

The connection integral changes continuously with perturbations of the Hamiltonian, while the curvature diverges at the degeneracy. This allows us to interpret this result in the degenerate case as half a quantum of Berry flux concentrated in a linelike flux tube along the line degeneracy.

APPENDIX F: EXAMPLE FOR FINITE LINEAR TOPOLOGICAL CHARGE DENSITY

In Eq. (11), we defined the linear topological charge density but showed later that it is either zero or is concentrated to single points akin to a Dirac delta. Here, we provide an example Hamiltonian with a degeneracy line in its parameter space, such that the degeneracy line carries a finite, continuously varying linear topological charge density.

Our example is a spin-1/2 Hamiltonian which is a nonlinear function of its parameters $\boldsymbol{B} = (B_x, B_y, B_z)$:

$$H(\boldsymbol{B}) = \left(B_x^2 - B_y^2\right) S_x + 2B_x B_y S_y + \left(B_x^2 + B_y^2\right) B_z S_z = \boldsymbol{B}_{\text{eff}} \cdot \boldsymbol{S}. \tag{F1}$$

We will call the quantity $\boldsymbol{B}_{\text{eff}}$ the *effective magnetic field*. The Hamiltonian in Eq. (F1) has a degeneracy line along the B_z axis. For small but finite B_x and/or B_y, the degenerate ground state splits in energy, quadratically in B_x and B_y. To calculate the linear topological charge density of the degeneracy line along the B_z axis, we follow the route introduced in Sec. III, utilizing Eq. (11).

We consider a cylinder of finite radius r surrounding the B_z axis. We parametrize the points of this cylinder with cylindrical coordinates, via $(B_x, B_y, B_z) = (r\cos\vartheta, r\sin\vartheta, s)$. At a given point of this cylinder, specified by (r, ϑ, s), the effective magnetic field reads

$$\boldsymbol{B}_{\text{eff}} = \begin{pmatrix} r^2\cos^2\vartheta - r^2\sin^2\vartheta \\ 2r^2\cos\vartheta\sin\vartheta \\ (r^2\cos^2\vartheta + r^2\sin^2\vartheta)s \end{pmatrix} = \begin{pmatrix} r^2\cos 2\vartheta \\ r^2\sin 2\vartheta \\ r^2 s \end{pmatrix}. \tag{F2}$$

The ground state can be expressed as

$$|\psi_0\rangle = \begin{pmatrix} \sin\frac{\vartheta_{\text{eff}}}{2} \\ -e^{i\varphi_{\text{eff}}}\cos\frac{\vartheta_{\text{eff}}}{2} \end{pmatrix}, \tag{F3}$$

where

$$\varphi_{\text{eff}} = 2\vartheta, \tag{F4}$$

$$\vartheta_{\text{eff}} = \tan^{-1}\left(\frac{1}{s}\right) \tag{F5}$$

are the spherical angles of the effective magnetic field. For this specific Hamiltonian, these angles do not depend on the radius r, hence the $r \to 0$ limit of Eq. (11) will be omitted below.

Having the ϑ and s dependence of the ground state $|\psi_0\rangle$ at hand, it is straightforward to calculate the two-dimensional Berry curvature according to Eq. (12),

$$\mathcal{B}_{2\text{D}}(s, \vartheta) = -2\,\text{Im}\,\langle \partial_\vartheta \psi | \partial_s \psi \rangle = \frac{1}{\sqrt{(s^2+1)^3}}, \tag{F6}$$

which depends only on s. From this, using Eq. (11), we evaluate the linear topological charge density,

$$\nu(B_z) \equiv \nu(s) = \frac{1}{\sqrt{(s^2+1)^3}}, \tag{F7}$$

which is indeed finite and depends continuously on the coordinate $B_z \equiv s$ along the degeneracy line.

APPENDIX G: SURFACE CHARGE DENSITY OF THE CHARGED ELLIPSOID

Here, we derive the surface charge density of the charged ellipsoid, a result quoted in the main text as Eq. (28). To do this, first we transform the Hamiltonian to a simple form, where the Berry curvature is easy to determine, then we transform it back to obtain the surface charge density.

1. Berry curvature in a simplified Hamiltonian

The Hamiltonian introduced in Eq. (3) can be simplified with the following steps. A global unitary transformation U which changes the right spin as $\boldsymbol{S}'_{\text{R}} = \hat{\boldsymbol{R}}\boldsymbol{S}_{\text{R}}$ changes the interaction to be isotropic:

$$H'(\boldsymbol{B}) = UH(\boldsymbol{B})U^\dagger = \boldsymbol{B} \cdot (\hat{\boldsymbol{g}}_{\text{L}}\boldsymbol{S}_{\text{L}} + \hat{\boldsymbol{g}}_{\text{R}}\hat{\boldsymbol{R}}^{-1}\boldsymbol{S}'_{\text{R}}) + J\boldsymbol{S}_{\text{L}} \cdot \boldsymbol{S}'_{\text{R}}. \tag{G1}$$

This transformation changes the right g tensor too. Now, we simplify the Zeeman term of the right spin with a linear transformation:

$$\boldsymbol{B}' = \hat{\boldsymbol{R}}\hat{\boldsymbol{g}}_{\text{R}}^{\text{T}}\boldsymbol{B}. \tag{G2}$$

To do this, we substitute the unit matrix $\hat{\boldsymbol{g}}_{\text{R}}\hat{\boldsymbol{R}}^{-1}\hat{\boldsymbol{R}}\hat{\boldsymbol{g}}_{\text{R}}^{-1}$; we get

$$H'(\boldsymbol{B}) = \boldsymbol{B} \cdot \hat{\boldsymbol{g}}_{\text{R}}\hat{\boldsymbol{R}}^{-1}\left(\hat{\boldsymbol{R}}\hat{\boldsymbol{g}}_{\text{R}}^{-1}\hat{\boldsymbol{g}}_{\text{L}}\boldsymbol{S}_{\text{L}} + \boldsymbol{S}'_{\text{R}}\right) + J\boldsymbol{S}_{\text{L}} \cdot \boldsymbol{S}'_{\text{R}}. \tag{G3}$$

This changes the left g tensor to a transformed $\hat{\boldsymbol{M}}$ matrix:

$$\hat{\boldsymbol{R}}\hat{\boldsymbol{g}}_{\text{R}}^{-1}\hat{\boldsymbol{g}}_{\text{L}} = \hat{\boldsymbol{g}}_{\text{L}}^{-1}\hat{\boldsymbol{g}}_{\text{L}}\hat{\boldsymbol{R}}\hat{\boldsymbol{g}}_{\text{R}}^{-1}\hat{\boldsymbol{g}}_{\text{L}} = \hat{\boldsymbol{g}}_{\text{L}}^{-1}\hat{\boldsymbol{M}}\hat{\boldsymbol{g}}_{\text{L}} = \hat{\boldsymbol{M}}'. \tag{G4}$$

The result is a Hamiltonian with $\hat{\boldsymbol{R}}' = \mathbb{1}_{3\times3}$ and $\hat{\boldsymbol{g}}'_{\text{R}} = \mathbb{1}_{3\times3}$

$$H'(\boldsymbol{B}') = \boldsymbol{B}' \cdot (\hat{\boldsymbol{M}}'\boldsymbol{S}_{\text{L}} + \boldsymbol{S}'_{\text{R}}) + J\boldsymbol{S}_{\text{L}} \cdot \boldsymbol{S}'_{\text{R}}. \tag{G5}$$

The global unitary transformation leaves the Berry curvature invariant but the linear transformation in the parameter space changes it, as we derive it in the next subsection.

For degeneracy ellipsoids, $\hat{\boldsymbol{M}} = a\mathbb{1}_{3\times 3}$ is proportional to the unit matrix:

$$H'(\boldsymbol{B}') = \boldsymbol{B}' \cdot (a\boldsymbol{S}_{\mathrm{L}} + \boldsymbol{S}'_{\mathrm{R}}) + J\boldsymbol{S}_{\mathrm{L}} \cdot \boldsymbol{S}'_{\mathrm{R}}. \tag{G6}$$

The result is an isotropic Hamiltonian. It has a degeneracy sphere with radius

$$R = \frac{1}{2}\left(1 + \frac{1}{a}\right), \tag{G7}$$

carrying a total topological charge 2. The Berry curvature in the transformed parameter space can be calculated using Gauss's law because of the isotropy

$$\boldsymbol{\mathcal{B}}'(\boldsymbol{B}') = \begin{cases} 0 & B' < R \\ \frac{\boldsymbol{B}'}{B'^3} & B' > R. \end{cases} \tag{G8}$$

2. Transformation of the Berry curvature in three-dimensional parameter space

To obtain an isotropic Hamiltonian, we did a global unitary transformation on the Hilbert space which preserves the Berry curvature, but we also did a linear transformation on the parameter space which, however, changes the curvature. In this subsection, we derive the transformation of the Berry curvature in three-dimensional parameter spaces.

We assume that Berry curvature with the transformed argument $\boldsymbol{x}'(\boldsymbol{x})$ is known; this transformed curvature is given by $\mathcal{B}'_i(\boldsymbol{x}') \equiv i\epsilon_{ijk}\langle\partial'_j\psi|\partial'_k\psi\rangle$, where ∂'_k is the derivative with respect to x'_k. We want to find the curvature with respect to the variable $\boldsymbol{x}$, given by $\mathcal{B}_i(\boldsymbol{x}) \equiv i\epsilon_{ijk}\langle\partial_j\psi|\partial_k\psi\rangle$. For the ith component, we get

$$\begin{aligned}\mathcal{B}_i(\boldsymbol{x}) &= i\epsilon_{ijk}\langle\partial_l\psi|\partial_m\psi\rangle \\ &= i\epsilon_{ijk}\langle\partial_j\psi(\boldsymbol{x}'(\boldsymbol{x}))|\partial_k\psi(\boldsymbol{x}'(\boldsymbol{x}))\rangle \\ &= i\epsilon_{ijk}(\partial_j x'_l)(\partial_k x'_m)\langle\partial'_l\psi|\partial'_m\psi\rangle,\end{aligned} \tag{G9}$$

where we used the chain rule. The partial derivative $\partial_j x'_l = J_{lj}$ is an element of the Jacobian matrix. This shows that the Berry curvature transforms as a two-form. Multiplying with the Jacobian from the left yields

$$\begin{aligned}J_{ni}\mathcal{B}_i(\boldsymbol{x}) &= i\epsilon_{ijk}J_{ni}J_{lj}J_{mk}\langle\partial'_l\psi|\partial'_m\psi\rangle \\ &= i(\det\hat{\boldsymbol{J}})\epsilon_{nlm}\langle\partial'_l\psi|\partial'_m\psi\rangle \\ &= (\det\hat{\boldsymbol{J}})\mathcal{B}'_n(\boldsymbol{x}'(\boldsymbol{x})),\end{aligned} \tag{G10}$$

where the Berry curvature with the transformed argument $\boldsymbol{\mathcal{B}}'(\boldsymbol{x}')$ appeared. From this, we write the transformation rule specific to three-dimensional parameter space:

$$\boldsymbol{\mathcal{B}}(\boldsymbol{x}) = (\det\hat{\boldsymbol{J}})\hat{\boldsymbol{J}}^{-1}\boldsymbol{\mathcal{B}}'(\boldsymbol{x}'(\boldsymbol{x})). \tag{G11}$$

For a linear transformation $\boldsymbol{x}'(\boldsymbol{x}) = \hat{\boldsymbol{J}}\boldsymbol{x}$, the Jacobian is the coefficient matrix.

3. Berry curvature in the parameter space of the ellipsoid

Now we can use the transformation of the Berry curvature derived in Eq. (G11) to the Berry curvature in Eq. (G8) with the transformation introduced in Eq. (G2):

$$\boldsymbol{\mathcal{B}}(\boldsymbol{B}) = (\det\hat{\boldsymbol{J}})\hat{\boldsymbol{J}}^{-1}\boldsymbol{\mathcal{B}}'(\boldsymbol{B}'(\boldsymbol{B})). \tag{G12}$$

Here $\hat{\boldsymbol{J}} = \hat{\boldsymbol{R}}\hat{\boldsymbol{g}}_{\mathrm{R}}^{\mathrm{T}}$. Outside the ellipsoid, we get

$$\begin{aligned}\boldsymbol{\mathcal{B}}(\boldsymbol{B}_{S+}) &= \det\left(\hat{\boldsymbol{R}}\hat{\boldsymbol{g}}_{\mathrm{R}}^{\mathrm{T}}\right)\left(\hat{\boldsymbol{R}}\hat{\boldsymbol{g}}_{\mathrm{R}}^{\mathrm{T}}\right)^{-1}\frac{\hat{\boldsymbol{R}}\hat{\boldsymbol{g}}_{\mathrm{R}}^{\mathrm{T}}\boldsymbol{B}_S}{\left|\hat{\boldsymbol{R}}\hat{\boldsymbol{g}}_{\mathrm{R}}^{\mathrm{T}}\boldsymbol{B}_S\right|^3} \\ &= \det(\hat{\boldsymbol{g}}_{\mathrm{R}})\frac{\boldsymbol{B}_S}{\left|\hat{\boldsymbol{g}}_{\mathrm{R}}^{\mathrm{T}}\boldsymbol{B}_S\right|^3};\end{aligned} \tag{G13}$$

inside we get

$$\boldsymbol{\mathcal{B}}(\boldsymbol{B}_{S-}) = 0. \tag{G14}$$

From Eq. (6), we get the equation for the degeneracy ellipsoid $\boldsymbol{B}_S = B_S\boldsymbol{b}$:

$$\left|\hat{\boldsymbol{g}}_{\mathrm{R}}^{\mathrm{T}}\boldsymbol{B}_S\right| = B_S\left|\hat{\boldsymbol{g}}_{\mathrm{R}}^{\mathrm{T}}\boldsymbol{b}\right| = B_S g_{\mathrm{R}} = \frac{1}{2}\left(1 + \frac{1}{a}\right). \tag{G15}$$

To get an expression for the surface normal of the ellipsoid, we consider the scalar field

$$f(\boldsymbol{B}) = \left(\hat{\boldsymbol{g}}_{\mathrm{R}}^{\mathrm{T}}\boldsymbol{B}\right)^2 \tag{G16}$$

that is constant on the degeneracy ellipsoid. Hence the gradient

$$\nabla f = 2\hat{\boldsymbol{g}}_{\mathrm{R}}\hat{\boldsymbol{g}}_{\mathrm{R}}^{\mathrm{T}}\boldsymbol{B} \tag{G17}$$

is proportional to the normal vector of the surface. Thus, the normal vector for the degeneracy ellipsoid at $\boldsymbol{B}_S$ reads

$$\boldsymbol{n}(\boldsymbol{B}_S) = \frac{\hat{\boldsymbol{g}}_{\mathrm{R}}\hat{\boldsymbol{g}}_{\mathrm{R}}^{\mathrm{T}}\boldsymbol{B}_S}{\left|\hat{\boldsymbol{g}}_{\mathrm{R}}\hat{\boldsymbol{g}}_{\mathrm{R}}^{\mathrm{T}}\boldsymbol{B}_S\right|}. \tag{G18}$$

The surface topological charge density is proportional to the jump of the normal component of the Berry curvature

$$\begin{aligned}\sigma(\boldsymbol{B}_S) &= \frac{1}{2\pi}[\boldsymbol{\mathcal{B}}(\boldsymbol{B}_{S+}) - \boldsymbol{\mathcal{B}}(\boldsymbol{B}_{S-})]\cdot\boldsymbol{n}(\boldsymbol{B}_S) \\ &= \frac{\det\hat{\boldsymbol{g}}_{\mathrm{R}}}{2\pi\left|\hat{\boldsymbol{g}}_{\mathrm{R}}^{\mathrm{T}}\boldsymbol{B}_S\right|\cdot\left|\hat{\boldsymbol{g}}_{\mathrm{R}}\hat{\boldsymbol{g}}_{\mathrm{R}}^{\mathrm{T}}\boldsymbol{B}_S\right|} \\ &= \frac{a\det\hat{\boldsymbol{g}}_{\mathrm{R}}}{\pi(a+1)\left|\hat{\boldsymbol{g}}_{\mathrm{R}}\hat{\boldsymbol{g}}_{\mathrm{R}}^{\mathrm{T}}\boldsymbol{B}_S\right|},\end{aligned} \tag{G19}$$

where in the last step Eq. (G15) was used.

This calculation shows that the topological surface charge density is finite if the degenerate surface separates the parameter space into two regions with different Berry curvatures.

[1] C. Herring, Accidental degeneracy in the energy bands of crystals, Phys. Rev. **52**, 365 (1937).

[2] M. V. Berry, Quantal phase factors accompanying adiabatic changes, Proc. R. Soc. London A **392**, 45 (1984).

[3] M. Z. Hasan and C. L. Kane, *Colloquium*: Topological insulators, Rev. Mod. Phys. **82**, 3045 (2010).

[4] N. P. Armitage, E. J. Mele, and A. Vishwanath, Weyl and Dirac semimetals in three-dimensional solids, Rev. Mod. Phys. **90**, 015001 (2018).

[5] J. K. Asbóth, L. Oroszlány, and A. Pályi, *A Short Course on Topological Insulators* (Springer, Heidelberg, 2016).

[6] R.-P. Riwar, M. Houzet, J. S. Meyer, and Y. V. Nazarov, Multi-terminal Josephson junctions as topological matter, Nat. Commun. **7**, 11167 (2016).

[7] Z. Scherübl, A. Pályi, G. Frank, I. E. Lukács, G. Fülöp, B. Fülöp, J. Nygård, K. Watanabe, T. Taniguchi, G. Zaránd, and S. Csonka, Observation of spin–orbit coupling induced Weyl points in a two-electron double quantum dot, Commun. Phys. **2**, 108 (2019).

[8] W. Wernsdorfer and R. Sessoli, Quantum phase interference and parity effects in magnetic molecular clusters, Science **284**, 133 (1999).

[9] P. Bruno, Berry Phase, Topology, and Degeneracies in Quantum Nanomagnets, Phys. Rev. Lett. **96**, 117208 (2006).

[10] V. Gritsev and A. Polkovnikov, Dynamical quantum Hall effect in the parameter space, Proc. Natl. Acad. Sci. **109**, 6457 (2012).

[11] G. Frank, Z. Scherübl, S. Csonka, G. Zaránd, and A. Pályi, Magnetic degeneracy points in interacting two-spin systems: Geometrical patterns, topological charge distributions, and their stability, Phys. Rev. B **101**, 245409 (2020).

[12] J. von Neumann and E. P. Wigner, Über das Verhalten von Eigenwerten bei adiabatischen Prozessen, Phys. Z. **30**, 467 (1929) [On the behaviour of eigenvalues in adiabatic processes].

[13] V. I. Arnold, Remarks on eigenvalues and eigenvectors of Hermitian matrices, Berry phase, adiabatic connections and quantum Hall effect, Selecta Math. **1**, 1 (1995).

[14] B. Simon, Holonomy, the Quantum Adiabatic Theorem, And Berry's Phase, Phys. Rev. Lett. **51**, 2167 (1983).

[15] C. Fang, M. J. Gilbert, X. Dai, and B. A. Bernevig, Multi-Weyl Topological Semimetals Stabilized by Point Group Symmetry, Phys. Rev. Lett. **108**, 266802 (2012).

[16] Z. Yan and Z. Wang, Floquet multi-Weyl points in crossing-nodal-line semimetals, Phys. Rev. B **96**, 041206(R) (2017).

[17] S. Ahn, E. J. Mele, and H. Min, Optical conductivity of multi-Weyl semimetals, Phys. Rev. B **95**, 161112(R) (2017).

[18] Z.-M. Huang, J. Zhou, and S.-Q. Shen, Topological responses from chiral anomaly in multi-Weyl semimetals, Phys. Rev. B **96**, 085201 (2017).

[19] B. Béri, Topologically stable gapless phases of time-reversal-invariant superconductors, Phys. Rev. B **81**, 134515 (2010).

[20] J.-M. Carter, V. V. Shankar, M. A. Zeb, and H.-Y. Kee, Semimetal and topological insulator in perovskite iridates, Phys. Rev. B **85**, 115105 (2012).

[21] C. Fang, Y. Chen, H.-Y. Kee, and L. Fu, Topological nodal line semimetals with and without spin-orbital coupling, Phys. Rev. B **92**, 081201(R) (2015).

[22] W. Wu, Y. Liu, S. Li, C. Zhong, Z.-M. Yu, X.-L. Sheng, Y. X. Zhao, and S. A. Yang, Nodal surface semimetals: Theory and material realization, Phys. Rev. B **97**, 115125 (2018).

[23] C. Fang, H. Weng, X. Dai, and Z. Fang, Topological nodal line semimetals, Chin. Phys. B **25**, 117106 (2016).

[24] T. Bzdušek, Q. Wu, A. Rüegg, M. Sigrist, and A. A. Soluyanov, Nodal-chain metals, Nature (London) **538**, 75 (2016).

[25] Q.-F. Liang, J. Zhou, R. Yu, Z. Wang, and H. Weng, Node-surface and node-line fermions from nonsymmorphic lattice symmetries, Phys. Rev. B **93**, 085427 (2016).

[26] Y.-M. Xie, X.-J. Gao, X. Y. Xu, C.-P. Zhang, J.-X. Hu, and K. T. Law, Kramers nodal line metals, Nat. Commun. **12**, 3064 (2021).

[27] K. Ono, D. G. Austing, Y. Tokura, and S. Tarucha, Current rectification by Pauli exclusion in a weakly coupled double quantum dot system, Science **297**, 1313 (2002), https://science.sciencemag.org/content/297/5585/1313.full.pdf.

[28] F. H. L. Koppens, C. Buizert, K. J. Tielrooij, I. T. Vink, K. C. Nowack, T. Meunier, L. P. Kouwenhoven, and L. M. K. Vandersypen, Driven coherent oscillations of a single electron spin in a quantum dot, Nature (London) **442**, 766 (2006).

[29] K. C. Nowack, F. H. L. Koppens, Y. V. Nazarov, and L. M. K. Vandersypen, Coherent control of a single electron spin with electric fields, Science **318**, 1430 (2007).

[30] J. R. Petta, A. C. Johnson, J. M. Taylor, E. A. Laird, A. Yacoby, M. D. Lukin, C. M. Marcus, M. P. Hanson, and A. C. Gossard, Coherent manipulation of coupled electron spins in semiconductor quantum dots, Science **309**, 2180 (2005).

[31] M. D. Schroer, K. D. Petersson, M. Jung, and J. R. Petta, Field tuning the g Factor in InAs Nanowire Double Quantum Dots, Phys. Rev. Lett. **107**, 176811 (2011).

[32] S. Nadj-Perge, S. M. Frolov, E. P. A. M. Bakkers, and L. P. Kouwenhoven, Spin-orbit qubit in a semiconductor nanowire, Nature (London) **468**, 1084 (2010).

[33] K. V. Kavokin, Symmetry of anisotropic exchange interactions in semiconductor nanostructures, Phys. Rev. B **69**, 075302 (2004).

[34] Y. Kato, R. C. Myers, D. C. Driscoll, A. C. Gossard, J. Levy, and D. D. Awschalom, Gigahertz electron spin manipulation using voltage-controlled g-tensor modulation, Science **299**, 1201 (2003), http://www.sciencemag.org/content/299/5610/1201.full.pdf.

[35] M. Veldhorst, R. Ruskov, C. H. Yang, J. C. C. Hwang, F. E. Hudson, M. E. Flatté, C. Tahan, K. M. Itoh, A. Morello, and A. S. Dzurak, Spin-orbit coupling and operation of multivalley spin qubits, Phys. Rev. B **92**, 201401(R) (2015).

[36] A. Crippa, R. Maurand, L. Bourdet, D. Kotekar-Patil, A. Amisse, X. Jehl, M. Sanquer, R. Laviéville, H. Bohuslavskyi, L. Hutin, S. Barraud, M. Vinet, Y.-M. Niquet, and S. De Franceschi, Electrical Spin Driving by g-Matrix Modulation in Spin-Orbit Qubits, Phys. Rev. Lett. **120**, 137702 (2018).

[37] S. D. Liles, F. Martins, D. S. Miserev, A. A. Kiselev, I. D. Thorvaldson, M. J. Rendell, I. K. Jin, F. E. Hudson, M. Veldhorst, K. M. Itoh, O. P. Sushkov, T. D. Ladd, A. S. Dzurak, and A. R. Hamilton, Electrical control of the g-tensor of a single hole in a silicon MOS quantum dot, Phys. Rev. B **104**, 235303 (2021).

[38] J. R. Petta, H. Lu, and A. C. Gossard, A coherent beam splitter for electronic spin states, Science **327**, 669 (2010).

[39] T. Tanttu, B. Hensen, K. W. Chan, C. H. Yang, W. W. Huang, M. Fogarty, F. Hudson, K. Itoh, D. Culcer, A. Laucht, A. Morello, and A. Dzurak, Controlling Spin-Orbit Interactions in Silicon Quantum Dots Using Magnetic Field Direction, Phys. Rev. X **9**, 021028 (2019).

[40] A. Wallraff, D. I. Schuster, A. Blais, L. Frunzio, R. S. Huang, J. Majer, S. Kumar, S. M. Girvin, and R. J. Schoelkopf, Strong coupling of a single photon to a superconducting qubit using circuit quantum electrodynamics, Nature (London) **431**, 162 (2004).

[41] Y. Kubo, F. R. Ong, P. Bertet, D. Vion, V. Jacques, D. Zheng, A. Dréau, J.-F. Roch, A. Auffeves, F. Jelezko, J. Wrachtrup, M. F. Barthe, P. Bergonzo, and D. Esteve, Strong Coupling of

a Spin Ensemble to a Superconducting Resonator, Phys. Rev. Lett. **105**, 140502 (2010).

[42] C. Janvier, L. Tosi, L. Bretheau, Ç. Ö. Girit, M. Stern, P. Bertet, P. Joyez, D. Vion, D. Esteve, M. F. Goffman, H. Pothier, and C. Urbina, Coherent manipulation of Andreev states in superconducting atomic contacts, Science **349**, 1199 (2015).

[43] L. Tosi, C. Metzger, M. F. Goffman, C. Urbina, H. Pothier, S. Park, A. L. Yeyati, J. Nygård, and P. Krogstrup, Spin-Orbit Splitting of Andreev States Revealed by Microwave Spectroscopy, Phys. Rev. X **9**, 011010 (2019).

[44] P. Roushan, C. Neill, Y. Chen, M. Kolodrubetz, C. Quintana, N. Leung, M. Fang, R. Barends, B. Campbell, Z. Chen, B. Chiaro, A. Dunsworth, E. Jeffrey, J. Kelly, A. Megrant, J. Mutus, P. J. J. O'Malley, D. Sank, A. Vainsencher, J. Wenner *et al.*, Observation of topological transitions in interacting quantum circuits, Nature (London) **515**, 241 (2014).

[45] T. Souza, M. Tomka, M. Kolodrubetz, S. Rosenberg, and A. Polkovnikov, Enabling adiabatic passages between disjoint regions in parameter space through topological transitions, Phys. Rev. B **94**, 094106 (2016).

[46] T. Curtright, Z. Cao, S. Huang, J. Sarmiento, S. Subedi, D. Tarrence, and T. Thapaliya, Charge densities for conducting ellipsoids, Eur. J. Phys. **41**, 035204 (2020).

[47] X.-Q. Sun, S.-C. Zhang, and T. Bzdusek, Conversion Rules for Weyl Points and Nodal Lines in Topological Media, Phys. Rev. Lett. **121**, 106402 (2018).

[48] R. González-Hernández, E. Tuiran, and B. Uribe, Topological electronic structure and Weyl points in nonsymmorphic hexagonal materials, Phys. Rev. Materials **4**, 124203 (2020).

[49] M. A. Wilde, M. Dodenhöft, A. Niedermayr, A. Bauer, M. M. Hirschmann, K. Alpin, A. P. Schnyder, and C. Pfleiderer, Symmetry-enforced topological nodal planes at the Fermi surface of a chiral magnet, Nature (London) **594**, 374 (2021).

[50] V. Fatemi, A. R. Akhmerov, and L. Bretheau, Weyl Josephson circuits, Phys. Rev. Research **3**, 013288 (2021).

[51] M. M. Hirschmann, A. Leonhardt, B. Kilic, D. H. Fabini, and A. P. Schnyder, Symmetry-enforced band crossings in tetragonal materials: Dirac and Weyl degeneracies on points, lines, and planes, Phys. Rev. Materials **5**, 054202 (2021).

[52] M. D. Schroer, M. H. Kolodrubetz, W. F. Kindel, M. Sandberg, J. Gao, M. R. Vissers, D. P. Pappas, A. Polkovnikov, and K. W. Lehnert, Measuring a Topological Transition in an Artificial Spin-1/2 System, Phys. Rev. Lett. **113**, 050402 (2014).

[53] I. Martin, G. Refael, and B. Halperin, Topological Frequency Conversion in Strongly Driven Quantum Systems, Phys. Rev. X **7**, 041008 (2017).

[54] S. Körber, L. Privitera, J. C. Budich, and B. Trauzettel, Interacting topological frequency converter, Phys. Rev. Research **2**, 022023(R) (2020).

[55] A. Garg, Berry phases near degeneracies: Beyond the simplest case, Am. J. Phys. **78**, 661 (2010).

[56] R. Wiesendanger, Spin mapping at the nanoscale and atomic scale, Rev. Mod. Phys. **81**, 1495 (2009).

[57] A. Spinelli, M. Gerrits, R. Toskovic, B. Bryant, M. Ternes, and A. F. Otte, Exploring the phase diagram of the two-impurity Kondo problem, Nat. Commun. **6**, 10046 (2015).

[58] R. A. Horn and C. R. Johnson, *Matrix Analysis* (Cambridge University Press, Cambridge, 1985).